*Istraživanja i projektovanja za privredu*
*ISSN 1451-4117*
*DOI:10.5937/jaes0-46531*
*www.engineeringscience.rs*

iipp publishing

*Journal of Applied Engineering Science*
*Vol. 23, No. 1, 2025*
*Original Scientific Paper*
*Paper number: 23(2025)1, 1249, 15-36*

# COMPARISON OF GAUSSIAN HEAT FLOW OF FSW RELYING ON VON MISES CRITERION AND CONSTITUTIVE MODELS OF YIELD STRENGTH

**Ghassan Shaker Abdul Ridha[1], Mohammed Abdulridha Abbas[2,3]*, Ramin Hashemi[4], Mohd Amri Lajis[3], Muhannad Ahmed[5]**

[1] *Middle Technical University, Technical Institute Kut, Department of Electrical Techniques, Baghdad, Iraq*
[2] *Al-Furat Al-Awsat Technical University (ATU), Engineering Technical College-Najaf, Aeronautical Techniques Engineering Department, Najaf, Iraq*
[3] *University Tun Hussein Onn Malaysia (UTHM Sustainable Manufacturing and Recycling Technology), Advanced Manufacturing and Materials Center (SMART-AMMC), Parit Raja, Malaysia*
[4] *Iran University of Science and Technology, School of Mechanical Engineering, Tehran, Iran*
[5] *Al-Furat Al-Awsat Technical University (ATU), Engineering Technical College-Najaf, Power Mechanics Techniques Engineering Department, Najaf, Iraq*

* *mohd.a.abbas@atu.edu.iq*

*In the Friction Stir Welding (FSW) operation, the role of thermal applied load modeling is no secret to simulate the heat distribution issued from this process. Unfortunately, the previous models implemented in transient mode did not present an accurate model for the moving heat source resulting from FSW operation. The main reason for this issue is attributed to the confidence and deviation ratios, especially with the Gaussian Distribution (GD). Besides, these models did not utilize the constitutive models of yield strength for comparison. Accordingly, the current study aims to present hybrid thermal models adopting 99.75% and 0.25% for confidence and deviation ratios, respectively, where it hybridized the Von Mises criterion with the constitutive models for yield strength to Voce, Hollomon, and Swift. Hence, these models contribute to presenting a comparison study to predict numerically the thermal history and investigate this history experimentally. Therefore, these hybrid models were used with finite element simulation to validate the experimental thermal history of FSW for Al 6061-T6 under 800 rpm, 10 mm/min, and 15 kN for rotational speed, linear velocity, and applied force sequentially. Finally, this validation has proved the dominance of the hybrid model for Von Mises-Voce in predicting the thermal history and peak temperature compared to other hybrid models.*

*Keywords: FSW, thermal history, constitutive models, von mises, strain hardening*

## 1 INTRODUCTION

The distinctive mixture of magnesium, silicon, copper, and chromium, besides the element of aluminum in Al 6061-T6 alloy, contributed to adoption in aerospace, marine, and military areas [1]. One of the reasons to adopt this alloy in these areas is the advanced mechanical properties, where it possesses an age-hardenable microstructure [2]. Consequently, it was exploited in various welding techniques, especially in the Friction Stir Welding (FSW) operation.

One of the early studies conducted in FSW of Al 6061-T6 alloy has tracked the longitudinal plunge behavior of pin-tool in the welding path. Thus, this behavior contributed to obtaining the friction peak temperature at 635 K and 156 rpm of the pin shoulder area with the workpiece. Accordingly, the friction zone changed yield point to tensive due to the temperature disparity between this area and the surroundings [3]. From here, the thermal history recorded by thermocouples has become vital to comprehending the heat distribution zones in the FSW line and interpreting the heat increase of the nugget distributed in the Thermomechanically Affected Zone (TMAZ) [4]. Furthermore, the growth of rotational velocity and dropping welding speed led to a rise in the heat by conduction in TMAZ compared to the Heat-Affected Zone (HAZ) and Base Material Zone (BMZ). This variation of velocities produced a gradient in hardness property based on the increasing size of grains in BMZ and even TMAZ, respectively [5-8]. Moreover, the contrast of thermal conductivity, specific heat, and thermal diffusivity among aluminum and magnesium elements in Al 6061 alloy during FSW also encouraged the experimental adoption of Zhang's models to interpret the heat generated in friction zones [9,10]. Other than that, the recrystallization phenomenon was responsible in the nugget region, at the high friction temperature, to efficiently flow material [11-13]. Therefore, these experimental studies have demonstrated the profound effect of heat distribution by the FSW technique on the morphology and properties of the welding zone of this alloy. Hence, it was essential to introduce a numerical interpretation and heat model of this operation. The brief survey in Table 1 describes the numerous numerical models of heat generated by this technique in Al 6061-T6 alloy.

Although other studies adopted the models mentioned above in Table 1 [14-19], the mode of each model and the shape of the pen tool revealed the variation of these models. Additionally, the welding velocity ($v_l$) in some models in Table 1 did not emphasize the coordinate system of the FSW path. Accordingly, the early and influential studies to overcome the path problem of FSW of Al 6061-T6 proposed employing the Gaussian Distribution (GD) method of heat generation [19,20]. Unfortunately, these proposed studies did not elucidate the deviation factor ($\sigma$), the confidence percentage, and the heat source. Therefore, this study aims to adopt these limitations and present a

hybrid heat generation model that contributes to creating an efficient path as a moving heat source. Moreover, it also focuses on employing the constitutive models of Hollomon, Swift, and Voce depending on the Von-Mises yield criterion to the maximum shear stress of the pin. Consequently, the Gaussian heat flow of the FSW operation of Al 6061-T6 is compared based on these constitutive models.

Table 1. A concise survey for the influential models of heat generation in FSW simulation applied to Al 6061-T6

| Reference No. | Model of heat generation in FSW | | Model Mode |
|---|---|---|---|
| [21,22] | $q_P = \left\{\left[\frac{2\pi t_W \tau r_P}{\sqrt{3}\sin(90°+\tan^{-1}\mu)}\left(v_l \sin\lambda + \frac{\mu \sin\emptyset}{\sqrt{(1+\mu^2)}}\right)\right] + \left[\frac{4\mu F_P \cos\emptyset \sin\lambda}{\pi \sin(90°+\tan^{-1}\mu)}\right]\right\}$ | (1) | THT# |
| | $\emptyset = 90° - \lambda - \tan^{-1}\mu$ | (1.1) | |
| | $q_s = \mu F_n v_l$ | (2) | |
| [23] | $q_{in} = \frac{\eta \mu F_n \omega}{30(r_S{}^2 - r_P{}^2)}$ | (3) | THT |
| [24] | $q_{in} = \begin{cases} \pi^2\omega\tau(r_S{}^3 - r_P{}^3)/45 & For\ pin\ shoulder \\ \pi^2\omega\tau r_P{}^3/45 & For\ pin\ bottom \\ \pi^2\omega\tau r_P{}^2 h_p/45 & For\ pin\ side \end{cases}$ | (4) | THT |
| [25-27] | $q_{in} = \begin{cases} Q_S/\pi(r_S{}^2 - r_P{}^2) & For\ pin\ shoulder \\ 2\omega r_P\left(\delta_c\tau + \mu P(1-\delta_c)\right)/3 & For\ pin\ bottom \\ Q_p \cos\lambda/2\pi \int_0^H (r_P + \delta_h \tan\lambda) dh_p & For\ pin\ side \end{cases}$ | (5) | UDF* |
| [28,29] | $q_{in} = \begin{cases} \mu\omega F_n r_S/A_S & For\ \ pin\ shoulder\ at\ T < T_m \\ \mu\omega r_p \tau/\sqrt{3(1+\mu^2)} & For\ pin\ at\ T < T_m \end{cases}$ | (6) | SSHT+ |
| [30] | $q_{in} = 4\pi^2\mu\omega P\left(r_S{}^2 + 3r_P{}^2 h_p\right)/3$ | (7) | THT |
| [31] | $dq_{in} = \psi v_l \mu P dA_s$ | (8) | EXP↓ |
| [32] | $q_{in} = q_f + q_{pd}$ | (9) | EXP |

#THT: Transient Heat Transfer; *UDF: User Define Function; +SSHT: Steady State Heat Transfer; ↓EXP: Explicit

To achieve this study, the welding velocity utilized in the current study is 10 mm/min. Besides, the rotational speed adopted is 800 rpm to implement the FSW of Al 6061-T6 alloy using a pin tool made from M1 Tool Steel. Furthermore, the thermal history is measured through six thermocouples' sensors placed by a distance identified in the Retreating Side (RS) and Advancing Side (AS). In turn, the experimental thermal outputs and Finite Element Analysis (FEA) outcomes exhibit the crucial hybrid model depending on one of the constitutive models as a planned methodology in the present work. Accordingly, in the succeeding chapters, numerical models, experimental setup, and procedures are demonstrated to comprehend the concept of the currently accredited methodology.

## 2 METHODOLOGY

The numerical simulation of the FSW operation was still a paramount goal for predicting the behavior of this operation to avoid a waste of time, exertion, and cost posed by the experimental tests [33]. Multiple models were developed to predict the heat distribution caused by friction in this welding technique, as demonstrated in Table 1. Therefore, it is essential to understand the methodological framework of the current numerical model, which includes the underlying hypotheses, boundary conditions, and a description of the hybrid nature of the model.

### 2.1 Model hypotheses

In preceding studies, the numerical models followed in the FSW simulation had usually differentiated due to the mode, properties, load distribution style, and applied load. In addition, these models have efficiently embraced many hypotheses to represent this simulation technique [33]. Thus, the present numerical simulation model assumes a symmetrical distribution of the work domain [26,29,30]. Moreover, the pin tool and shoulder are wholly immersed inside the workpiece [15,18]. Wherein the longitudinal socket resulting is regular and without protuberances [34,35]. Besides, the heat analysis in this model is in conduction transient mode and applied as a GD style of the heat generated [19,20,30]. Additionally, the thermal properties of this assumed model are as a temperature's function [25,30,32]. Likewise, this proposed model adopts the constitutive models of yield strength (Hollomon, Swift, and Voce) to specify the shear yield strength depending on the Von-Mises criterion [27,32,36,37].

According to these hypotheses, the model of numerical simulation utilized in the current study is symmetric, as depicted in Fig. 1. Additionally, the workpiece is fully exposed to plunge along the FSW path by the pin and shoulder

during the tool progression. As described in Fig. 1, the protuberances induced by the progress of the plunged tool are also neglected to construct a regular volumetric region in bright red, recognized as the welding zone. Depending on this description, the applied thermal load in Fig. 1 indicates the boundary conditions used in this study relying on these hypotheses. Hence, it is necessary to understand these conditions in the model embraced in this work.

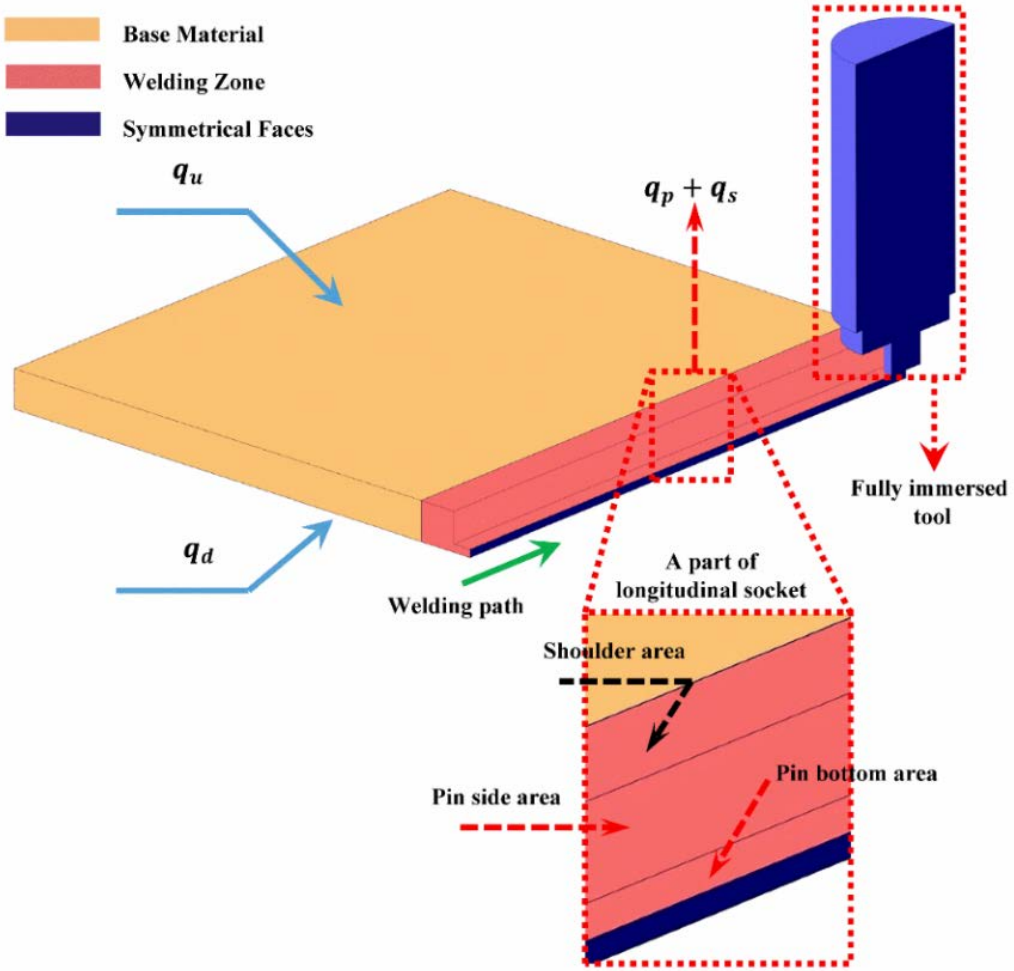


Fig. 1. Proposed model of FSW adopted in the current study

### 2.2 Boundary conditions

The simulation based on the FEA technique is deemed one of the effective solution methods to represent the thermal distribution of the FSW process. As a numerical solution, this technique in the previous studies permanently depended on the presented assumptions and the boundary conditions. The adopted hypotheses have been elementary described of thermal simulation in this study. Thus, there is a need to highlight the boundary conditions utilized in the current work.

In this article, the modeling of thermal simulation requires estimating the thermal loads as boundary conditions besides the heat source of the friction zone, as portrayed in Fig. 1. These loads are concentrated at up and down surfaces of Al 6061-T6 and are comprised of radiation and convection together simultaneously. Assuming a perfect effect of these loads at each of the upper, lower, and welding zones separately, Eq. (10) indicates this distribution of these applied loads [38,39]:

$$q = \begin{cases} h_u(T_o - T) + \varepsilon_r \sigma_{sb}\left({T_a}^4 - T^4\right), & at\ upper\ zone \\ q_{in,} & at\ welding\ zone \\ h_l(T_o - T) + \varepsilon_r \sigma_{sb}\left({T_a}^4 - T^4\right), & at\ lower\ zone \end{cases} \quad (10)$$

where $q_{in}$ is the heat source in the welding zone generated from friction between the pin tool and workpiece, $T$ is the temperature absorbed by upper and lower faces, $T_o$ refers to the reference temperature, $T_a$ denotes ambient temperature, $\varepsilon_r$ is the emissivity factor of surface, while $\sigma_{sb}$ is the Stefan-Boltzmann constant. Moreover, $h_u$ and $h_l$ are the convection heat transfer coefficients for the upper and lower zone surfaces, respectively.

For precisely accomplishing FSW simulation, measuring the ambient temperature utilizing the Extech-Environmental Meter model EN300 as a multifunction instrument was substantial. The reference temperature was 47˚C, as reported by this instrument. Accordingly, Table 2 refers to the thermal properties of Al 6061-T6 and atmospheric air at 47˚C. From here, the coefficients $h_u$ and $h_l$ were calculated according to Eq. (10) as follows [40-42]:

Table 2. Thermal properties of FSW medium [43-46]

| Property | Al 6061-T6 at 25˚C-426.7˚C | Air at 47˚C |
|---|---|---|
| Thermal conductivity ($k$) (W/m.K) | 167-233 | $27.861\times10^{-3}$ |
| Density ($\rho$) (kg/m$^3$) | 2700-2602 | 1.1032 |
| Heat capacity ($C_p$) (J/kg.K) | 896-1133 | 1007 |
| Kinematic viscosity ($v_k$) (m$^2$/s) | - | $17.592\times10^{-6}$ |
| Prandtl number ($P_r$) | - | 0.70524 |

$$Gr = \frac{g\theta\Delta T\delta^3}{{v_k}^2}, \tag{11}$$

$$Ra = Gr\ Pr, \tag{12}$$

$$Nu_u = \begin{cases} 0.54\ Ra^{0.25}\ 10^4 < Ra < 10^7, \\ 0.15\ Ra^{0.33}\ 10^7 < Ra < 10^{11}, \end{cases} \ For\ upper\ face \tag{13}$$

$$Nu_l = 0.27Ra^{0.25} \quad 10^5 < Ra < 10^{11},\ For\ lower\ face \tag{14}$$

$$h = \begin{cases} \mathrm{Nu}_u k/\delta\,, & For\ upper\ face \\ \mathrm{Nu}_l k/\delta\,, & For\ lower\ face \end{cases} \tag{15}$$

where $Gr$ refers to the Grashof number, $g$ is the gravitational acceleration constant, $\delta$ indicates the characteristic length of the horizontal plate, $\theta$ denotes the volume expansion coefficient, and $v_k$ is the kinematic viscosity of air. Besides, $Ra$ and $Pr$ are the numbers of Rayleigh and Prandtl sequentially. On the other hand, $Nu_u$ and $Nu_l$ are the Nusselt numbers for the upper and lower surfaces, respectively. Remarkably, $Gr$, $Pr$, and $Nu$ numbers are dimensionless numbers applied in the thermal analysis of FSW. From here, Eqs. (11)-(15) have presented a mathematical interpretation to assess Eq. (10) based on the isothermal behavior of the horizontal plate for upper and lower surfaces. This assessment was aimed to determine the convection coefficients in Eq. (15). Hence, this thermal context has been exploited in the simulation implemented in this article.

According to these facts, it turned out that the thermal boundaries applied on the upper and lower surfaces of Al 6061-T6 contributed to identifying the heat loads on these surfaces. As a thermal boundary, the heat source in the welding zone described in Fig. 1 and Eq. (10) has not been observably elucidated. Consequently, highlighting this source is the main objective of the present study due to its role in enhancing the thermal model in this zone concerning the welding path and constitutive models of yield strength

### 2.2.1 Welding zone boundaries

After sorting the models utilized to calculate the heat distribution resulting from the friction mechanism for welding Al 6061-T6 and presenting them as a survey in Table 1, it was discovered that these models were noticeably lacking in the coordinate system of the welding path. In contrast, the moving heat source for this welding path based on other models did not include the confidence percentage and mean of absolute deviation factor according to GD principles [19,20]. As is well known, the friction heat in FSW simulation, as a principal source of heat, is an influential part of the transient mode of heat conduction based on Fourier's expression apprised in Eq. (16) [47]:

$$\nabla(k\nabla T) + Q_{in} = \rho C_p \frac{\partial T}{\partial t}, \tag{16}$$

where $\nabla(k\nabla T)$ refers to thermal conductivity at $x$, $y$, and $z$ directions, $Q_{in}$ is the heat source input at the welding zone (W/m$^3$), as exhibited in Fig. 1, and $t$ is FSW duration. According to Eqs. (10) and (16), it can be expressed the heat in this zone as follows:

$$\int_0^h Q_{in}\, dh_d = q_{in} = q_p + q_s, \tag{17}$$

where $h_d$ is the depth of the welded plate, $q_p$ is the heat flux in the contact zone of the pin tool, and $q_s$ indicates the heat flux applied in the shoulder contact region. From Eq. (6), it can be redrafted to Eq. (17) to be as follows:

$$q_{in} = \mu\omega\left(r_p\tau/\sqrt{3(1+\mu^2)} + F_n r_s/A_s\right), \tag{18}$$

where $\mu$ is the friction coefficient, $\omega$ is the angular velocity, $r_p$ and $r_s$ are the radiuses of the pin and shoulder, respectively, $F_n$ denotes normal force, and $A_s$ is the surface area of the shoulder. On the other side, $\tau$ refers to the average of maximum shear yield stress, which can be calculated based on the Von Mises principle [27,32]:

$$\tau = \sigma_y/\sqrt{3}, \tag{19}$$

where $\sigma_y$ is the yield stress of Al 6061-T6 welded by FSW operation. This stress has adopted the constitutive models of Hollomon, Swift, and Voce to enhance the Von Mises criterion in Eq. (19) and to specify the average of maximum shear yield stress. This enhancement contributed to establishing a hybrid model among these constitutive models and this criterion separately. Hence, this criterion in Eq. (19) can be revised to be [36]:

$$\tau = K_h(0.002)^{n_h}/\sqrt{3}, \quad (20)$$

$$\tau = K_s{\varepsilon_o}^{n_s}/\sqrt{3}, \quad (21)$$

$$\tau = \sigma_o(1-C)/\sqrt{3}, \quad (22)$$

where $K_h$ and $K_s$ are the strength coefficients according to constitutive models of Hollomon and Swift sequentially, and $n_h$ and $n_s$ are the strain-hardening exponents depending on the constitutive models of Hollomon and Swift, respectively. Furthermore, $\varepsilon_o$ and $\sigma_o$ indicate the saturation of the strain and stress, respectively, and $C$ is the material coefficient based on the constitutive model of Voce. According to Eqs. (20)-(22), the heat flux in the welding zone in Eq. (18) can be reformulated to build the subsequent hybrid models:

$$q_{in} = \mu\omega\left(r_p K_h(0.002)^{n_h}/3\sqrt{1+\mu^2} + F_n r_S/A_S\right), \quad (23)$$

$$q_{in} = \mu\omega\left(r_p K_s{\varepsilon_o}^{n_s}/3\sqrt{1+\mu^2} + F_n r_S/A_S\right), \quad (24)$$

$$q_{in} = \mu\omega\left(r_p \sigma_o(1-C)/3\sqrt{1+\mu^2} + F_n r_S/A_S\right), \quad (25)$$

These hybrid formulas of heat flux in the welding zone need to weld path to be adopted as influential models in FEA simulation. For this reason, the GD model is adopted in the current work to overcome the welding path problem in Eqs. (23)-(25) depending on the Model of Probability Density (MPD) demonstrated below [48,49]:

$$D_p(r) = e^{-(r^2/2\sigma^2)}/\sqrt{2\pi}\sigma, \quad (26)$$

where $\sigma$ is the standard deviation and $r$ is the random variable. As depicted in Fig. 2, behaviorally, the curve of the GD model did not statistically approach zero. Consequently, hypothetically, this curve was fully distributed on the friction zone resulting from the FSW process to represent the heat flux for both the shoulder and pin. On the other hand, the deviation and confidence percentages employed in the current work are 0.25% and 99.75%, respectively. The mechanism for using these percentages was based on the value of the t-test and the value issued from the Table of the student's T-Distribution to specify the best standard deviation. If the T-Distribution value is higher than the value calculated by the t-test procedure, then the deviation percentage assumed can be adopted as a significant condition [50,51]. Besides, it has been adopted 482˚C-493.3˚C and 800-1000 rpm as a range for peak temperatures and rotational speed, respectively, from FSW operation for Al 6061-T6, depending on previous studies, as factors to build a source of variation [52-54]. Hence, the outcome of this analysis led to the adopted 0.25% for the deviation percentage under this condition. Unfortunately, the other assumed percentages for the standard deviation contribute to maximizing the t-test value to the T-distribution value. Accordingly, these percentages are known as hypothetical for the best level of resolution according to GD, where these percentages operated at the symmetrical directions of the standard deviations ($3\sigma$,-$3\sigma$) [55-57]. By contrast, recruiting the under percentages for 99.75% contributes to restricting the heat distribution shoulder resulting from the path of FSW. Therefore, these percentages for the confidence and deviation are preferred in the thermal fluxes adopting the Gaussian model for distribution [58,59]. As a consequence, the distribution of the curve's shoulder ($R$) for friction-heat in Fig. 2 was assumed as below:

$$R = 3\sigma, \quad (27)$$

Consequently, Eq. (26) is:

$$D_p(r) = n\, e^{-(ar^2/bR^2)}/R, \quad (28)$$

where $n$, $a$, and $b$ represent the empirical constants and are equal to 1.1968, 8.1, and 2, individually. This function in Eq. (28) indicates the heat flow produced from friction between the pin and shoulder for the pin tool with the workpiece sequentially. Thus, this function leads to the following:

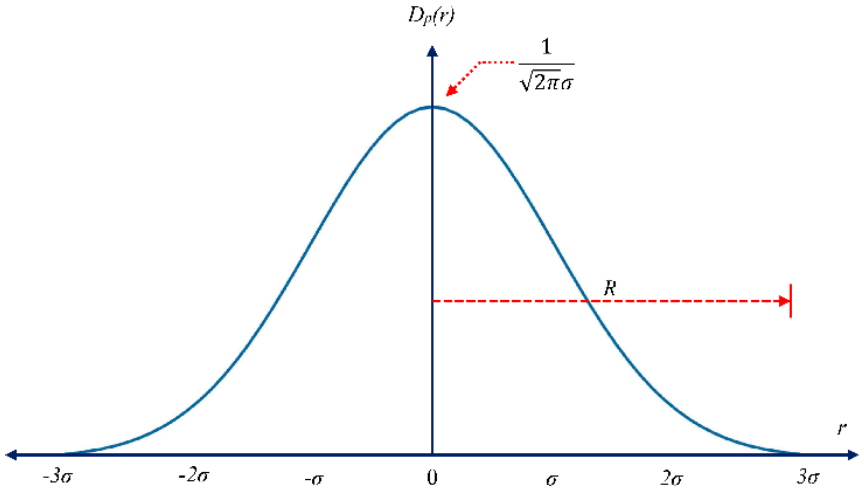

Fig. 2. GD model adopted for the heat friction in FSW

$$q(r) = D_p(r) = \begin{cases} q_p(r) \\ q_s(r) \end{cases}, \tag{29}$$

According to Eqs. (28) and (29), the maximum heat friction generated by FSW operation is:

$$q(r) = n/R = q_c \;\; at\; r = 0, \tag{30}$$

From Eqs. (28)-(30), the final formula of Eq. (28) is:

$$q(r) = q_c e^{-(ar^2/bR^2)}, \tag{31}$$

Hence, the friction energy flow in the welding zone is:

$$Q(r) = \int_0^R q(r)\, dA = \int_0^R q_c e^{-(ar^2/bR^2)}\, 2\pi r dr = 0.6903 R^2 q_c, \tag{32}$$

As a result of this procedure, the GD model of heat friction distribution in Eq. (32) represents a final function yielded from this distribution. Note that Eq. (32) can be utilized in the contact regions for pin and shoulder zones, respectively. In the contact zone of the pin, as remarked in Fig. 1, the friction energy is:

$$Q_p(r) = 2\pi r_p h_p q_p, \tag{33}$$

where $h_p$ denotes the pin height, hence the part related to the pin in Eqs. (23)-(25) is exploited in Eq. (33) to be:

$$Q_p(r) = 2\pi h_p \mu\omega\, {r_p}^2 K_h (0.002)^{n_h}/3\sqrt{1+\mu^2}, \tag{34}$$

$$Q_p(r) = 2\pi h_p \mu\omega\, {r_p}^2 K_s {\varepsilon_o}^{n_s}/3\sqrt{1+\mu^2}, \tag{35}$$

$$Q_p(r) = 2\pi h_p \mu\omega\, {r_p}^2 \sigma_o (1-C)/3\sqrt{1+\mu^2}, \tag{36}$$

From Eq. (32), the peak heat flux intensity in pin ($q_c$) depends on Eqs. (34)-(36) and Eq. (31) to lead to:

$$Q_p(r) = \left[3.0340 h_p \mu\omega\, K_h (0.002)^{n_h}/\sqrt{1+\mu^2}\right] e^{-(ar^2/b{r_p}^2)} \;\; at\; R = r_p, \tag{37}$$

$$Q_p(r) = \left[3.0340 h_p \mu\omega\, K_s {\varepsilon_o}^{n_s}/\sqrt{1+\mu^2}\right] e^{-(ar^2/b{r_p}^2)} \;\; at\; R = r_p, \tag{38}$$

$$Q_p(r) = \left[3.0340 h_p \mu\omega\, \sigma_o (1-C)/\sqrt{1+\mu^2}\right] e^{-(ar^2/b{r_p}^2)} \;\; at\; R = r_p, \tag{39}$$

The area of the pin shoulder contact region is:

$$A_S = \pi\left({r_S}^2 - {r_p}^2\right), \tag{40}$$

As the procedure followed in Eq. (33), the friction energy in the pin shoulder zone is also:

$$Q_s(r) = A_S q_s, \tag{41}$$

In accordance with Eqs. (23) to (25), the corresponding part for the pin shoulder is adjusted in Eq. (41) as follows:

$$Q_s(r) = \mu\omega r_s F_n, \tag{42}$$

From Eqs. (31) and (42), the ultimate heat flux in the pin shoulder ($q_c$) in Eq. (32) leads to:

$$Q_s(r) = [1.4486\mu\omega F_n/r_s]e^{-(ar^2/br_s{}^2)} \ \ at\ R = r_s, \tag{43}$$

In the same vein, Eqs. (37)-(39) and Eq. (43) can be revised as Eqs. (23)-(25) to be:

$$Q_{in}(r) = \mu\omega\left[\left(3.0340h_p\, K_h(0.002)^{n_h}e^{-(ar^2/br_p{}^2)}/\sqrt{1+\mu^2}\right) + \left(1.4486F_n e^{-(ar^2/br_s{}^2)}/r_s\right)\right], \tag{44}$$

$$Q_{in}(r) = \mu\omega\left[\left(3.0340h_p\, K_s\varepsilon_o{}^{n_s}e^{-(ar^2/br_p{}^2)}/\sqrt{1+\mu^2}\right) + \left(1.4486F_n e^{-(ar^2/br_s{}^2)}/r_s\right)\right], \tag{45}$$

$$Q_{in}(r) = \mu\omega\left[\left(3.0340h_p\, \sigma_o(1-C)e^{-(ar^2/br_p{}^2)}/\sqrt{1+\mu^2}\right) + \left(1.4486F_n e^{-(ar^2/br_s{}^2)}/r_s\right)\right], \tag{46}$$

where:

$$r^2 = x^2 + y^2, \tag{47}$$

where $x$ and $y$ are the coordinates of the FSW path based on the final hybrid models in Eqs. (44)-(46). As demonstrated, these hybrid models have relied on GD and the constitutive models of Hollomon, Swift, and Voce. Consequently, these models are employed in FEA to investigate the experimental outcomes of the FSW process for Al 6061-T6 and compare to select the best hybrid model. For this investigation, the full parameters in Table 3 of Hollomon, Swift, and Voce were utilized in these hybrid Eqs. (44)-(46), as influential data of shear yield strength.

Table 3. Full parameters of Al 6061 according to the constitutive models: Hollomon, Swift, and Voce [36]

| Material | Hollomon | | Swift | | | Voce | |
|---|---|---|---|---|---|---|---|
| Al 6061 | $K_h$ (MPa) | $n_h$ | $K_s$ (MPa) | $\varepsilon_o$ | $n_s$ | $\sigma_o$ (MPa) | $\sigma_o C$ (MPa) |
| | 347 | 0.0505 | 372 | 0.0054 | 0.0738 | 306 | 49 |

The simulation in the present work employs COMSOL traditional software, specifically utilizing the heat transient physics mode. Besides, a mesh size between 0.5-3 mm was chosen for the symmetric workpiece, as illustrated in Fig. 3. The numerical model for this study has been fully established to conduct finite element analysis (FEA) according to the proposed hypotheses and boundary conditions. Therefore, this simulation adopts transient thermal models, as outlined in Eqs. (44)-(46), introducing a novel heat flux path based on GD principles. Accordingly, this approach also moves away from relying on constant heat flow, computational fluid dynamics (CFD), or the explicit models listed in Table 1 that were used in previous studies.

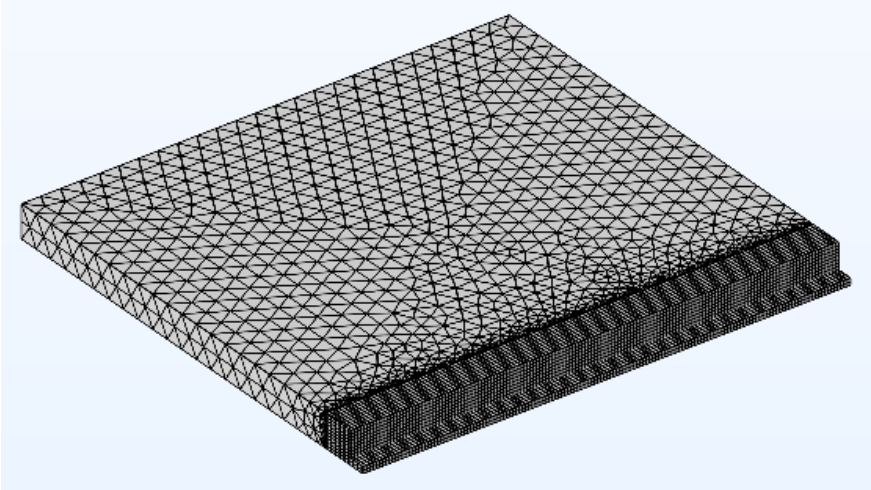

Fig. 3. Symmetric modeling mesh for welded part

## 3 EXPERIMENTAL SETUP AND PROCEDURES

Depending on the numerical models utilized in this work, it is becoming evident that there is a need to highlight the experimental circumstances and procedures of the FSW process to present a complete vision of the methodology of the existing research. Therefore, the main intent of these models is to compare and validate the empirical outcomes produced from these procedures. At this point, the details of the pin tool, the material of the workpiece, and work parameters have been included as a description of the experimental surroundings.

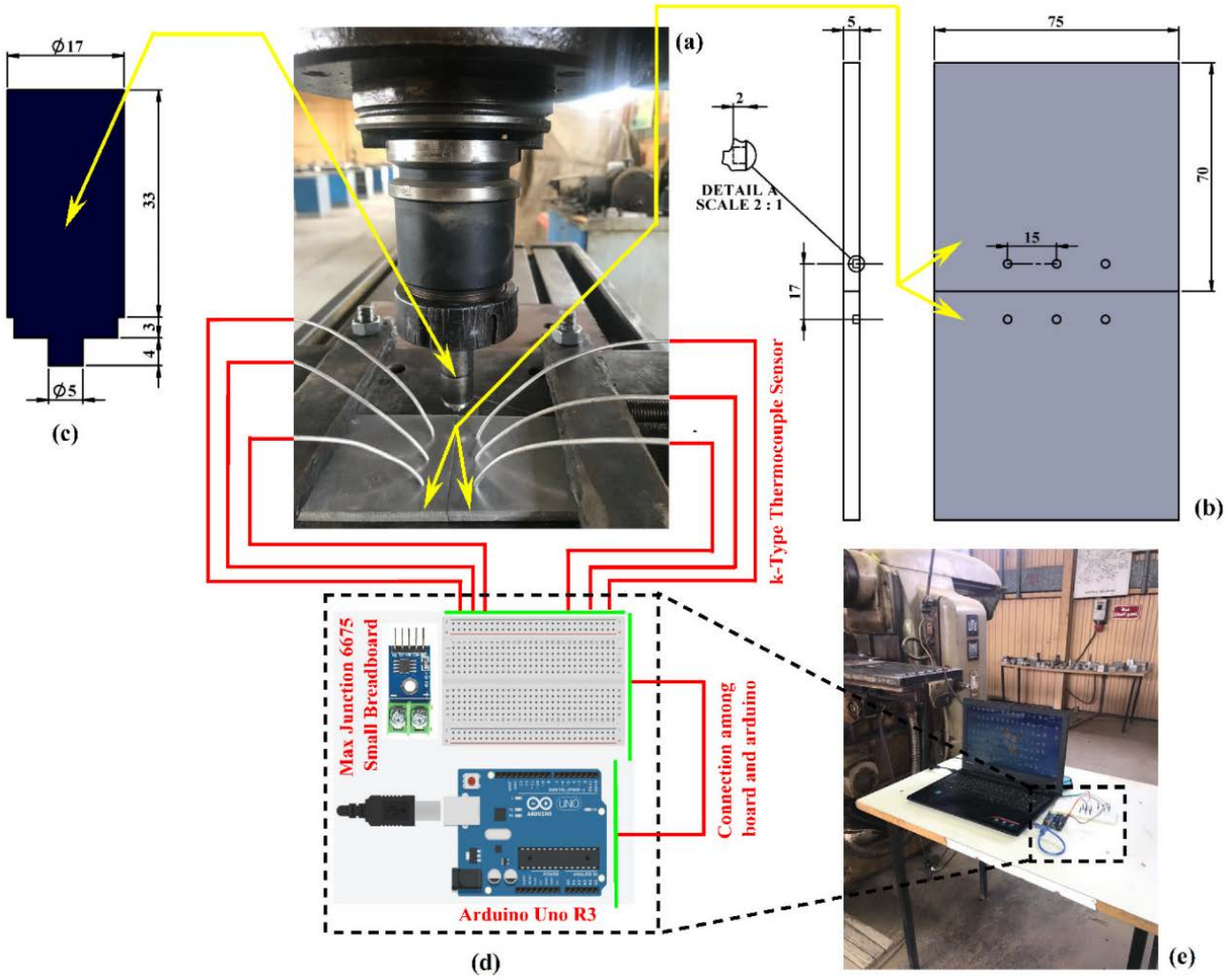


Fig. 4. FSW operation environment of Al 6061-T6: (a) Setup of work materials and thermocouple sensors, (b) Workpiece dimensions, (c) Pin tool dimensions, (d) Connection configuration for Arduino-Max Junction-small breadboard with workpiece by K-Type thermocouple sensors, (e) Connection configuration between Arduino and computer

As an operation tool, the material of the pin tool in Fig. 4(a) is made from M1 Tool Steel, where this tool was installed in the holder of the milling machine model (Commercial Semi-Automatic Milling Machine, India). The dimensions of this tool, as represented in Fig. 4(c), were designed to achieve the FSW job in the current experimental environment. At the same time, Al 6061-T6 alloy has been utilized as a workpiece and prepared by Wire-EDM Machine model (EX-40, Exeteck, India), where this machine has conducted the cutting operations of this workpiece according to the dimensions depicted in Fig. 4(b). Hence, overlapping these work materials leads to welding operation counting on the stir friction mechanism at 800 rpm and 10 mm/min for rotational and linear velocities, respectively. Besides, the force applied during FSW operation is 15 kN to supply sufficient pressure during the welding of Al 6061-T6 [29]. Meanwhile, the standard chemical composition of these materials has been validated using the Scanning Electron Microscopy/Energy Dispersive X-ray Spectroscopy (SEM/EDS) model (Jeol-JSM-6360LV, USA). The weight percentages of the elements of these work materials by EDS-Test in Fig. 5(a) and (b) were extremely close to the standard chemical composition.

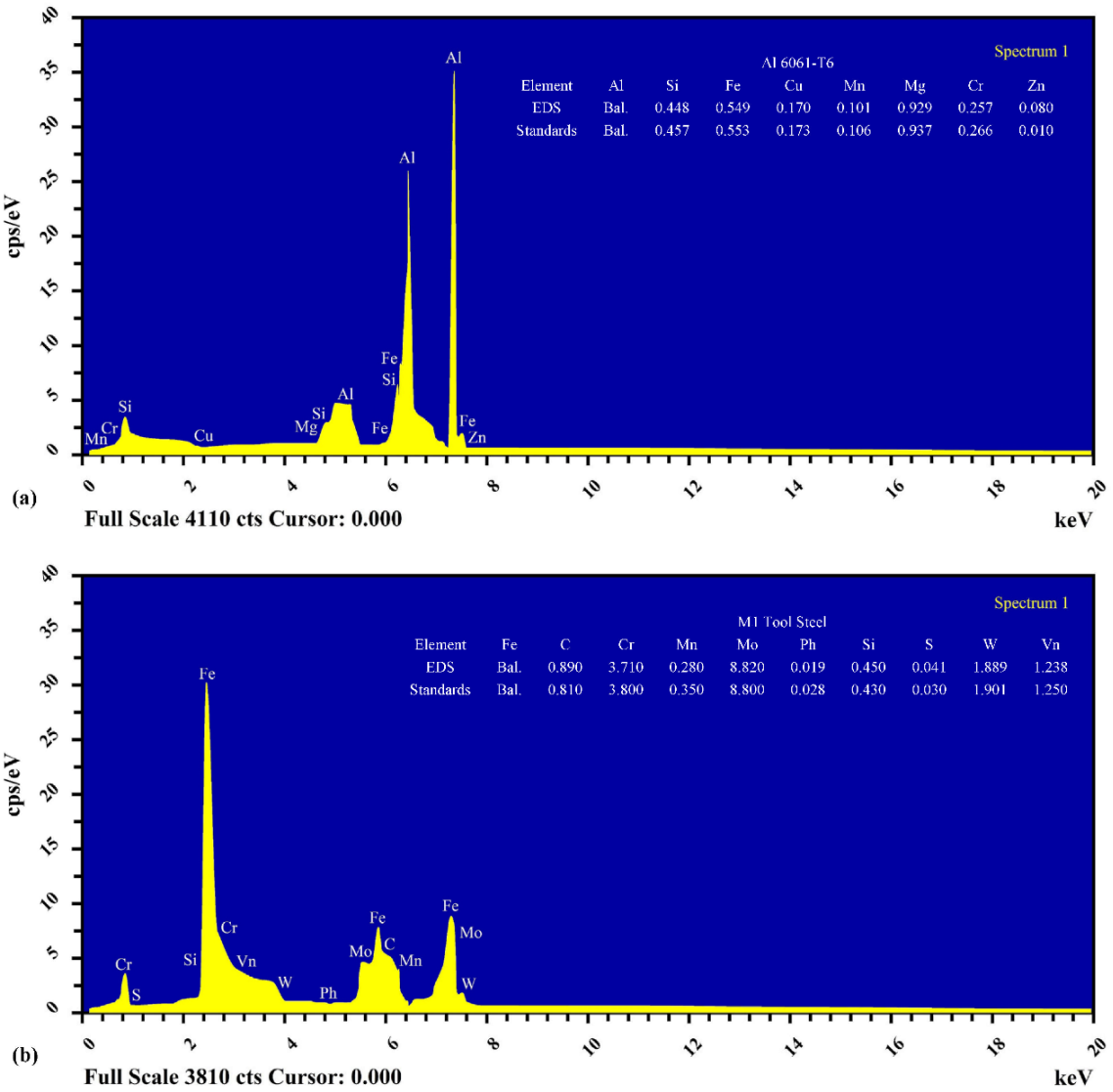


Fig. 5. Chemical composition comparison between EDS observation and the standard: (a) Workpiece: Al 6061-T6, (b) Pin tool: M1 Tool Steel

Usually, the thermal history demonstrates the heat distribution in the horizontal direction for the line of FSW operation. Consequently, to perform this job, six wire sensors used with the high-temperature thermocouple instrument model (K-Type-CR07) were exploited and distributed on workpieces, as indicated in Fig. 4(a) and (b). In turn, these wires connect with MAX-Junction model 6675, a small breadboard, and Arduino model (UNO-R3) as a thermal network instead of K-Type-CR07, as displayed in Fig. 4(d) and (e), to notate the thermal history. It is essential to compare the issued measurements between this network and K-Type-CR07 to avoid any uncertain measurements, where the error ratio of thermal history issued was 1.2%. Therefore, this step aimed to reduce the experimental cost in the current work and present a reliable and alternative method to record the thermal history. As a specification, the package K-Type-CR07 presents a thermal measurement up to 1300˚C with an error of 0.4%, while the MAX-Junction model 6675 does up to 1024˚C with an error of 0.25%. Contextually, the Arduino-Software version IDE 2.1.1 plays a significant role in obtaining the final thermal history report based on the traditional MATLAB-Toolbox version Ra2022. In addition, these sensors were fixed in the holes illustrated in Fig. 4(b) using cement (Omegabond 600) to avoid any vibration during the FSW process. Unfortunately, the Joining-Line resulting from the stir friction between the compressed plates of the workpiece and pin tool makes it difficult to install these sensors [60,61]. Therefore, to specify the peak temperature in this line, this study embraced the following empirical model [14,62]:

$$T_P = T_m \lambda (\omega^2 / v_l \times 10^4)^{\gamma}, \tag{48}$$

where $T_P$, $T_m$, $\omega$, and $v_l$ are peak temperature, melting temperature, angular velocity, and linear velocity of FSW operation, respectively. In addition, $\lambda$ and $\gamma$ denote the empirical constants, which equals 0.7 and 0.05 sequentially.

As a current methodology, the setup procedures for work materials, Arduino, and thermocouples have been explained to conduct friction welding by stir mechanism. Moreover, it presented the empirical model adopted to determine the peak temperature in the welding line. Hence, the thermal history is validated with the numerical simulation based on Eqs. (44)-(46) to pick the finest hybrid model based on Von Mises criterion and constitutive models of yield strength. In Fig. 6, this methodology can be briefly remarked, as aforementioned.

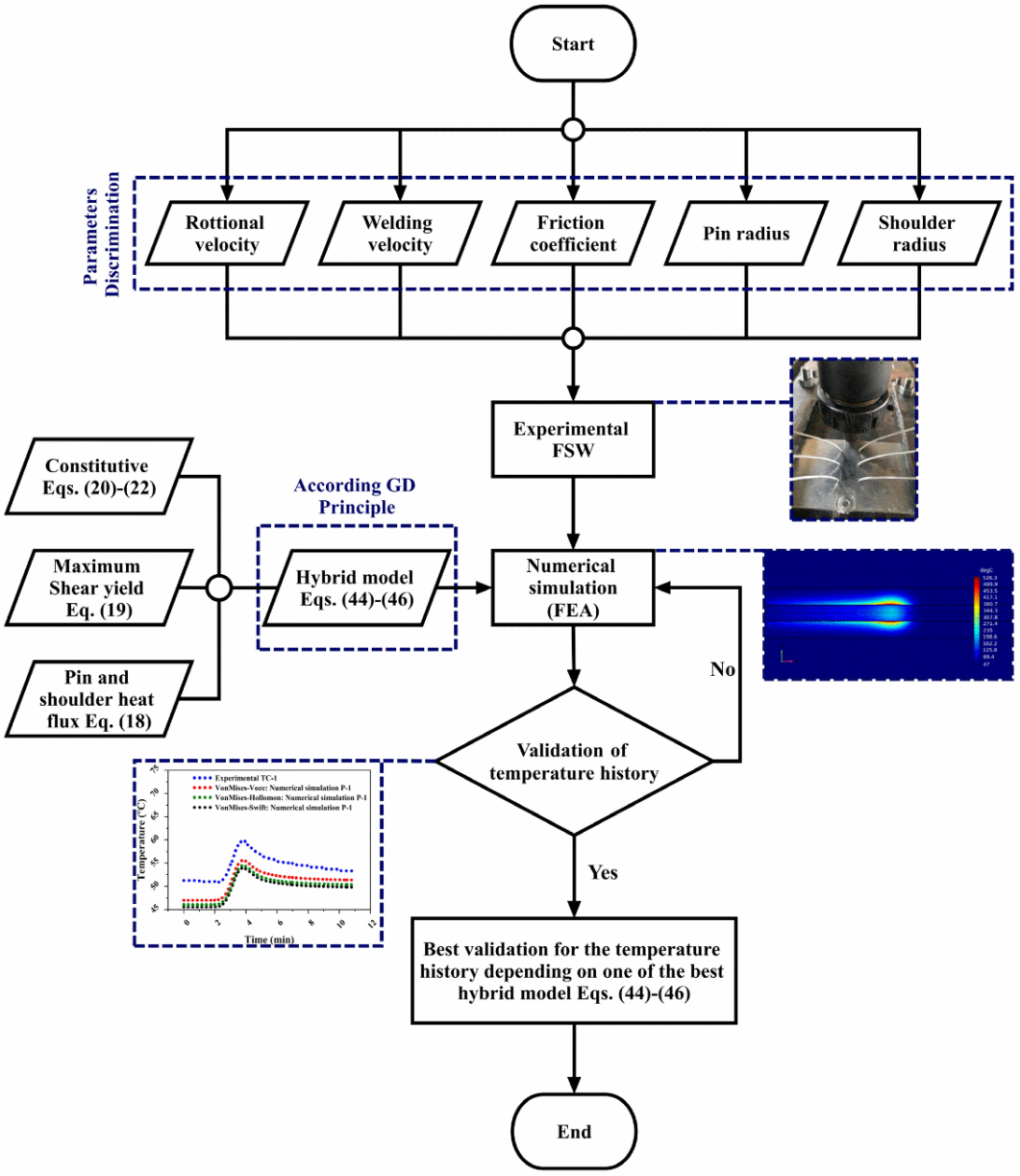


Fig. 6. Investigation methodology flowchart of hybrid models for FSW of Al 6061-T6

## 4 RESULTS AND DISCUSSION

After demonstrating both numerical models and experimental procedures as methodology utilized in the current study, the outcomes of this planned methodology can be remarked through thermal history and peak temperature depending on Eqs. (44)-(46). Therefore, this methodology is sensed by focusing on the thermal history issued by thermocouples sensors (TC1 to TC6) and the Prob-Points of FEA simulation (P-1 to P-6), respectively. Hence, this sensing will display how interdependent the experimental and numerical outcomes for this study are besides the behavior of these outcomes.

### 4.1 Thermal history and hybrid models

The thermal history produced from thermocouple sensors TC1 and TC4 and COMSOL Prob-Points P-1 and P-4 in Fig. 7(a) sequentially were acceptably close. Behaviorally, the temperature data of these Prob-Points in Fig. 7(a) was slightly less than the thermal history estimated by these thermocouples. In addition, points P-1 and P-4 have resulted from the FSW simulation of Al 6061-T6, as depicted in Fig. 7(b)-(d), depending on the hybrid models described in Eqs. (44)-(46) for the heat applied: Von Mises-Voce, Von Mises-Hollomon, and Von Mises-Swift sequentially. Therefore, the points P-1 and P-4 attributed to Von Mises-Voce in Fig. 7(a) and (b) are approximately matched with thermocouple points TC1 and TC4, as compared to Von Mises-Hollomon and Von Mises-Swift in Fig. 7(a), (c), and (d). As a result of these data, the maximum and average temperatures can be recognized based on these hybrid models in Table 4. Numerically and experimentally, the maximum temperature of thermal history was reported at 3.82 min, as illustrated in Fig. 7 and Table 4. Otherwise, along 11 min as the welding period, the average temperature was computed by P-1, P-4, and TC1, TC4, respectively.

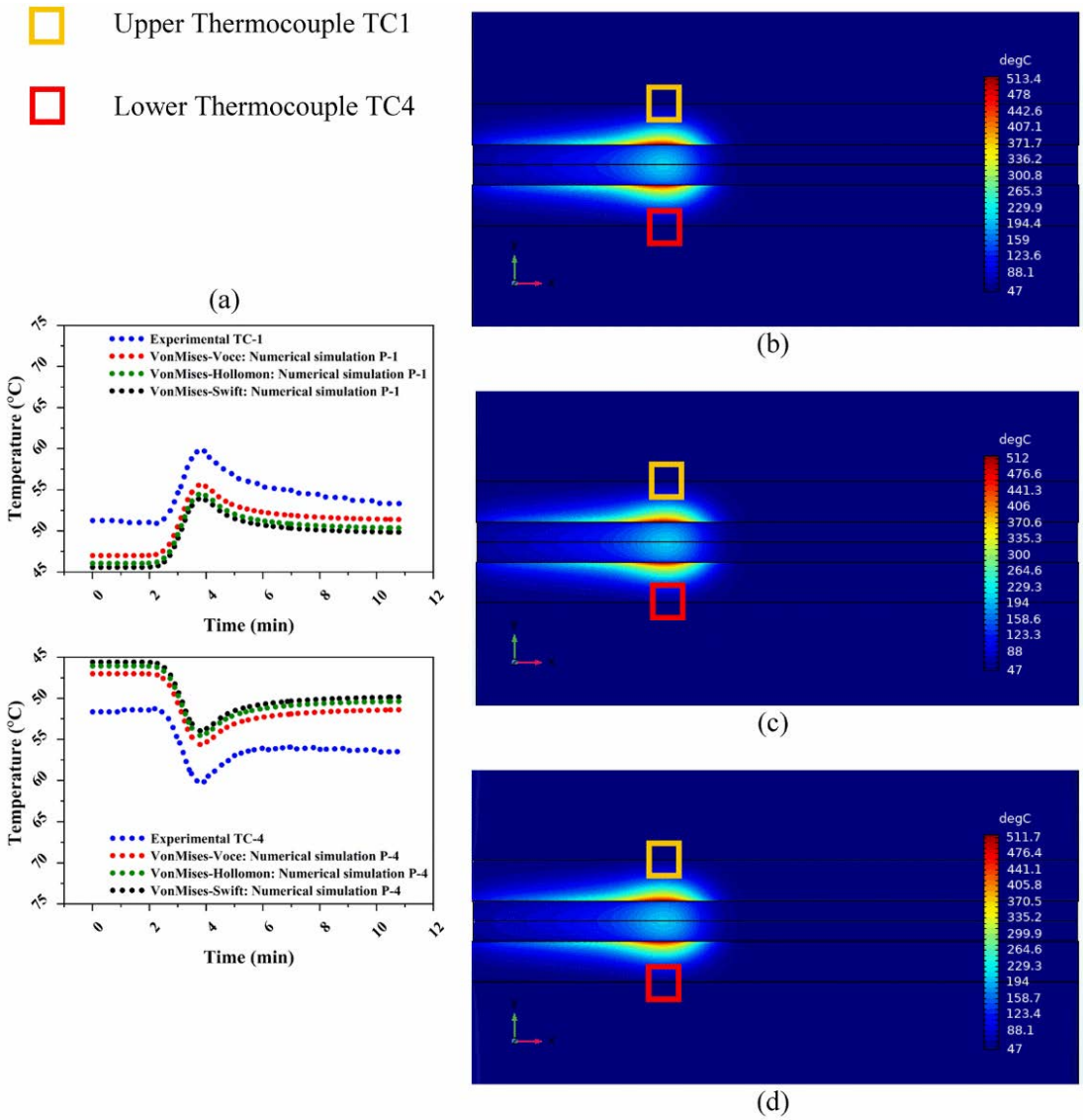


Fig. 7. Thermal history reported of FSW for Al 6061-T6. Observed (a) Comparison among thermal history measured by TC1 and TC4, reported by P-1 and P-4 according to hybrid models (b) Von Mises-Voce, (c) Von Mises-Hollomon, and (d) Von Mises-Swift

Observably, the thermal history according to the Von Mises-Voce model described in Eq. (46) is more precise compared to other hybrid models in Eqs. (44) and (45), as depicted in Fig. 7(a)-(d). As evidence, the error ratio (%$\epsilon$) according to Eq. (49) in Table 4 for the maximum and average temperatures estimated by TC1 and TC4 to P-1 and P-4 are not more than 8%, consecutively [63,64].

$$\%\epsilon = (|T_{P-n} - TCn| \,/TCn\,) \times 100, \tag{49}$$

where $T_{P\text{-}n}$ and $TCn$ are the measured temperatures resulting from COMCOL Prob-Points and thermocouples' sensors for the thermal network. From here, the strain-hardening behavior in the zone of FSW is the main reason for this variance in the thermal history. As demonstrated in Eq. (22), Voce's model is not fully saturated by this behavior depending on how much this zone expanded based on the friction between the pin tool and the workpiece. In turn, the active growth of grains in the FSW zone indicates excellent annealing behavior during this operation, which contributes to developing this zone. Therefore, Voce's model is stable and homogeny toward strain-hardening. On the contrary, the exponents of strain-hardening nh and ns for Hollomon and Swift in Eqs. (20) and (21), successively, are over zero, which contributes to increasing this saturation [65-67].

Table 4. Comparison of thermal history reported by P-1 and P-4, thermocouple sensors TC1 and TC4

| Hybrid model | Temperature case | COMSOL Temperatures (℃) | | Thermocouple Temperatures (℃) | | Time (min) | Error ratio %ϵ |
|---|---|---|---|---|---|---|---|
| Von Mises-Voce | Maximum | P-1 | 55.638 | TC1 | 59.808 | 3.82 | 6.972 |
| | | P-4 | 55.638 | TC4 | 60.252 | | 7.657 |
| | Average | P-1 | 51.021 | TC1 | 54.281 | 11 | 6.005 |
| | | P-4 | 51.021 | TC4 | 55.438 | | 7.967 |
| Von Mises-Hollomon | Maximum | P-1 | 54.525 | TC1 | 59.808 | 3.82 | 8.833 |
| | | P-4 | 54.525 | TC4 | 60.252 | | 9.504 |
| | Average | P-1 | 50.001 | TC1 | 54.281 | 11 | 7.885 |
| | | P-4 | 50.001 | TC4 | 55.438 | | 9.808 |
| Von Mises-Swift | Maximum | P-1 | 53.969 | TC1 | 59.808 | 3.82 | 9.763 |
| | | P-4 | 53.969 | TC4 | 60.252 | | 10.428 |
| | Average | P-1 | 49.491 | TC1 | 54.281 | 11 | 8.825 |
| | | P-4 | 49.491 | TC4 | 55.438 | | 10.728 |

In Table 4 and Fig. 7, the maximum temperatures reported by TC1 and TC4 are over 47˚C for the surrounding temperature measured by Extech-Environmental Meter-EN300 and reach 60˚C. These outcomes indicate TC1 and TC4 are distant neighbors from the FSW zone, as revealed in Fig. 7. Additionally, the welding time and lower coefficient of heat transitivity of air are insufficient to augment the thermal distribution produced from FSW operation [14]. Furthermore, the grain size at 800 rpm in the FSW zone was improved, as previously proven [68-70]. Hence, this contributed to enhancing and concentrating the temperature absorption in this zone. Accordingly, these reasons led to semi-restrictions on flowing the temperatures to TC1 and TC4.

According to these outcomes, it can observe these behaviors and interpretations for thermocouples (TC2, TC5); (TC3, TC6) besides the Prob-Points (P-2, P-5); (P-3, P-6), respectively. These thermocouples and Prob-Points have presented the same proof that the Von Mises-Voce model was dominant in the investigation with experimental thermal history, as demonstrated in Fig. 8, Table 5, and Fig. 9, Table 6. Although the percentage of error ratio (%ϵ) in other hybrid models employed in the simulation of FSW of Al 6061-T6 did not exceed 13% [71,72].

### *4.2 Peak temperature and hybrid models*

As previously reported, the thermal history was easily measured by TC1 to TC6 at neighbored points described in Figs. 7-9 compared to the pin and shoulder regions depicted in Fig. 1. To comprehend this case, the plunging and friction mechanisms during FSW of Al 6061-T6 are predominant in this zone and lead to friction and plastic deformation [32,73]. Hence, the measurement of thermal history is often complicated in these regions and causes to damage the thermocouple sensors by the pin tool [14,73]. Therefore, the model proposed by Arbegast and Hartley described in Eq. (48) contributed to overcoming this limitation by presenting the empirical peak temperature ranging from 0.6-0.9 from the melted point of Al 6061-T6 [74]. In contrast, the maximum temperature in Figs. 7-9 was remarkably concentrated in the shoulder than the pin. To justify this case, the area of friction and plastic deformation together in the shoulder is even more than that at the pin tool [75,76]. Accordingly, the peak temperature at 8.7 min in Fig. 10 also follows the similar behavior of maximum temperatures produced by thermocouples at the shoulder.

At 12.3-56.25 mm of the shoulder morphology in Fig. 10, the Shoulder Boundary Waves (SBW), as a boundary to pitched weld crowns, of FSW operation in yellow color largely conformed with the heat distribution resulting by simulation from ~ 250℃ to 521℃ and from ~ 250℃ to 528℃ for Von Mises-Voce and Von Mises-Hollomon, individually. However, this boundary does not conform to Von Mises-Swift from ~ 250℃ to 538℃. As aforementioned, the role of strain-hardening behavior contributes to producing an unstable hybrid model of thermal applied according to Hollomon and Swift and leads to an increase of error ratio, as depicted in Fig. 10 (b) and (c), up to 3.92% and 5.89%, successively, according to Eq. (50) [63,64,67].

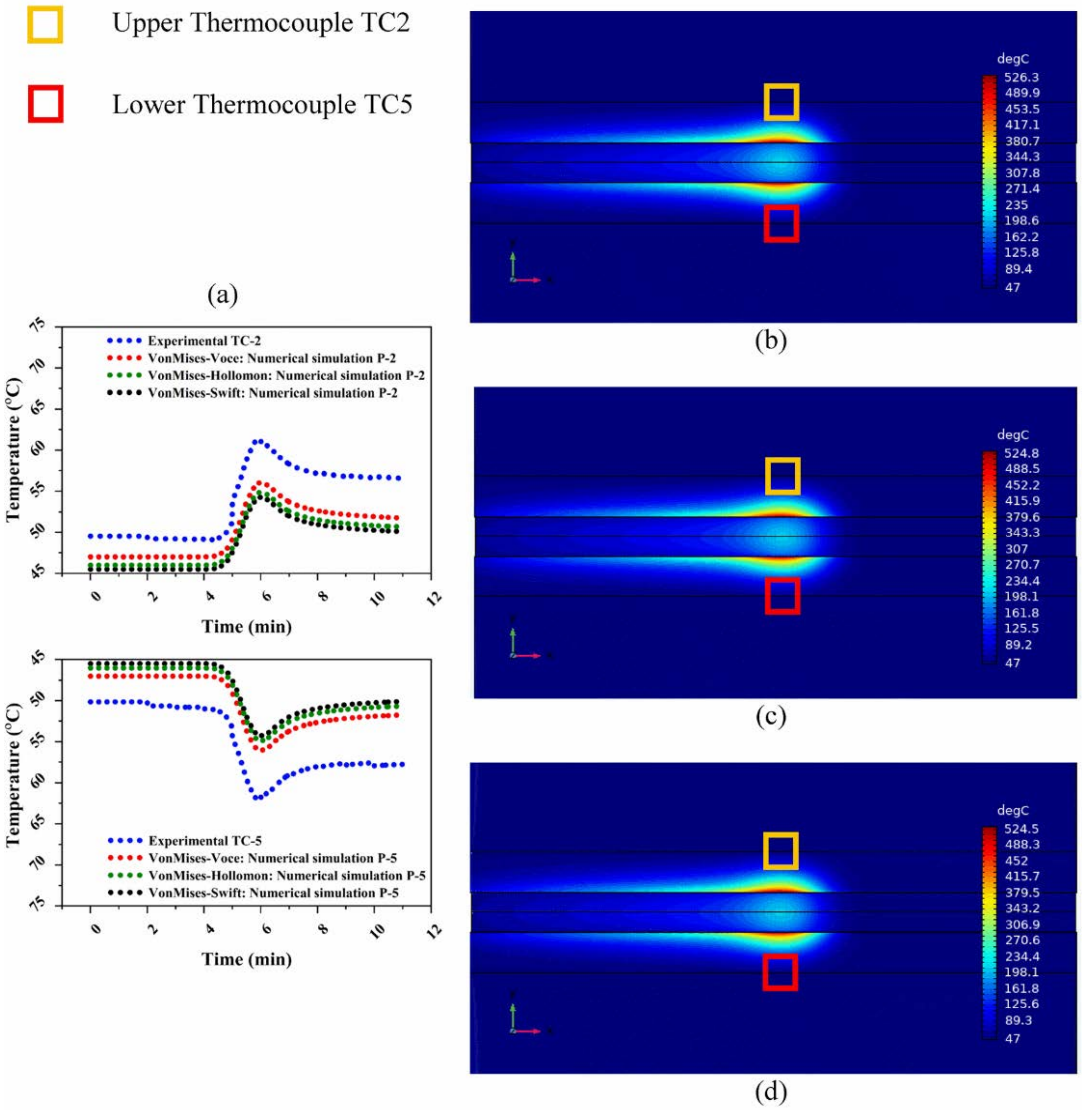


Fig. 8. Thermal history reported of FSW for Al 6061-T6. Observed (a) Comparison among thermal history measured by TC2 and TC5, reported by P-2 and P-5 according to hybrid models (b) Von Mises-Voce, (c) Von Mises-Hollomon, and (d) Von Mises-Swift

Table 5. Comparison of thermal history reported by P-2 and P-5, thermocouple sensors TC2 and TC5

| Hybrid model | Temperature case | COMSOL Temperatures (℃) | | Thermocouple Temperatures (℃) | | Time (min) | Error ratio %ϵ |
|---|---|---|---|---|---|---|---|
| Von Mises-Voce | Maximum | P-2 | 56.056 | TC2 | 61.434 | 6.01 | 8.754 |
| | | P-5 | 56.056 | TC5 | 62.209 | | 9.891 |
| | Average | P-2 | 50.279 | TC2 | 53.916 | 11 | 6.746 |
| | | P-5 | 50.279 | TC5 | 54.979 | | 8.550 |
| Von Mises-Hollomon | Maximum | P-2 | 54.878 | TC2 | 61.434 | 6.01 | 10.670 |
| | | P-5 | 54.878 | TC5 | 62.209 | | 11.784 |
| | Average | P-2 | 49.223 | TC2 | 53.916 | 11 | 8.704 |
| | | P-5 | 49.223 | TC5 | 54.979 | | 10.470 |
| Von Mises-Swift | Maximum | P-2 | 54.262 | TC2 | 61.434 | 6.01 | 11.674 |
| | | P-5 | 54.262 | TC5 | 62.209 | | 12.775 |
| | Average | P-2 | 48.670 | TC2 | 53.916 | 11 | 9.730 |
| | | P-5 | 48.670 | TC5 | 54.979 | | 11.476 |

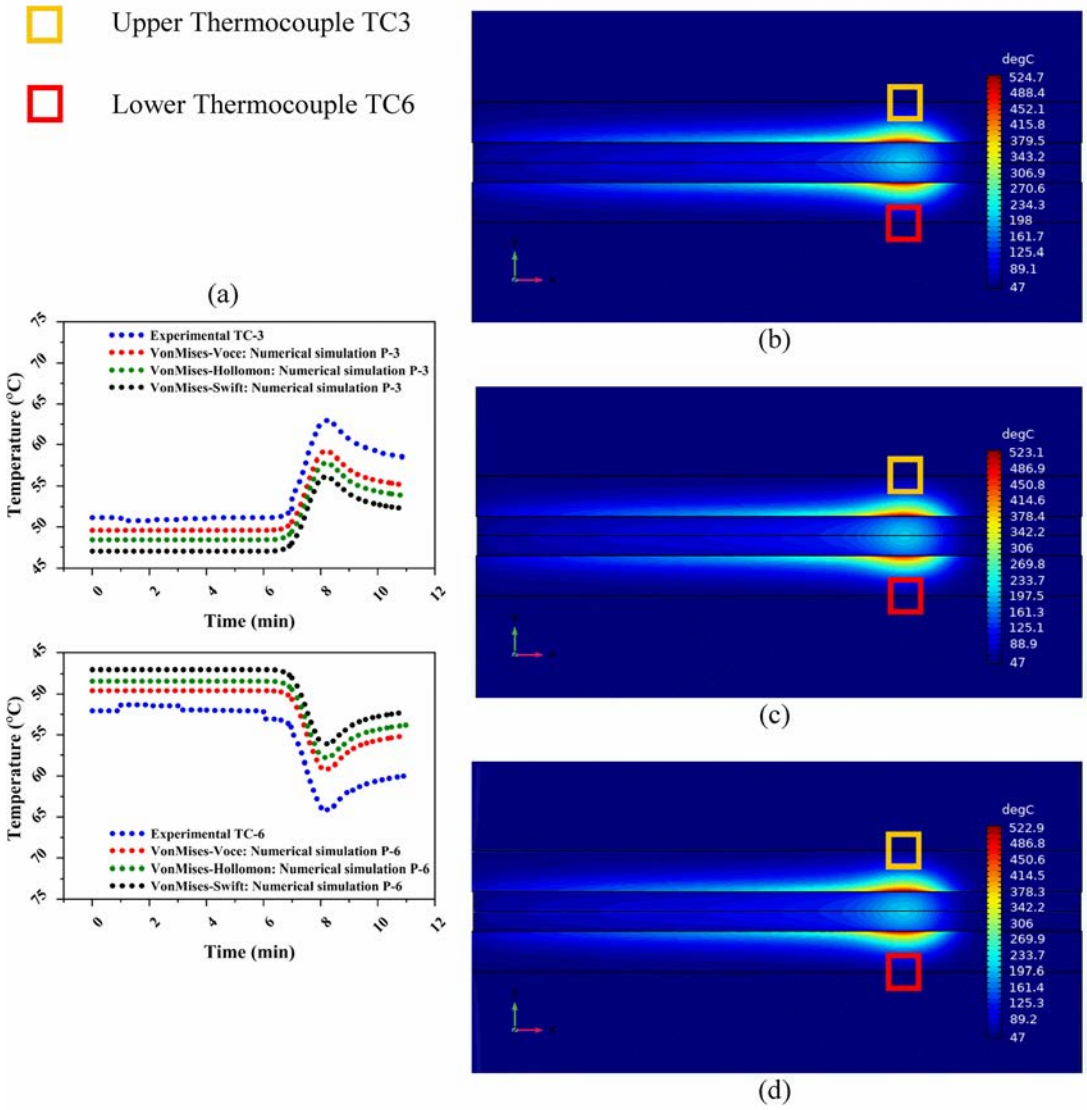


Fig. 9. Thermal history reported of FSW for Al 6061-T6. Observed (a) Comparison among thermal history measured by TC3 and TC6, reported by P-3 and P-6 according to hybrid models (b) Von Mises-Voce, (c) Von Mises-Hollomon, and (d) Von Mises-Swift

Table 6. Comparison of thermal history reported by P-3 and P-6, thermocouple sensors TC3 and TC6

| Hybrid model | Temperature case | COMSOL Temperatures (°C) | | Thermocouple Temperatures (°C) | | Time (min) | Error ratio %ϵ |
|---|---|---|---|---|---|---|---|
| Von Mises-Voce | Maximum | P-3 | 59.203 | TC3 | 62.971 | 8.18 | 5.984 |
| | | P-6 | 59.203 | TC6 | 64.128 | | 7.680 |
| | Average | P-3 | 52.004 | TC3 | 54.205 | 11 | 4.062 |
| | | P-6 | 52.004 | TC6 | 55.267 | | 5.904 |
| Von Mises-Hollomon | Maximum | P-3 | 57.800 | TC3 | 62.971 | 8.18 | 8.947 |
| | | P-6 | 57.800 | TC6 | 64.128 | | 10.949 |
| | Average | P-3 | 50.771 | TC3 | 54.205 | 11 | 6.764 |
| | | P-6 | 50.771 | TC6 | 55.267 | | 8.854 |
| Von Mises-Swift | Maximum | P-3 | 56.116 | TC3 | 62.971 | 8.18 | 10.885 |
| | | P-6 | 56.116 | TC6 | 64.128 | | 12.493 |
| | Average | P-3 | 49.293 | TC3 | 54.205 | 11 | 9.063 |
| | | P-6 | 49.293 | TC6 | 55.267 | | 10.810 |

$$\%\epsilon_P = (|T_{PS} - T_P| / T_P) \times 100, \quad (50)$$

where $T_{PS}$ is the peak temperature issued from COMSOL-Prob, and $T_P$ is the peak temperature according to Eq. (48) based on the empirical model of Arbegast and Hartley [74]. Hence, these peak temperatures are 508.07℃ and 521℃ for TPs at the shoulder and TP, respectively. Accordingly, the value of %ϵp between the predicted and empirical model according to Eq. (48) produced 2.54%, as illustrated in Fig. 10(a).

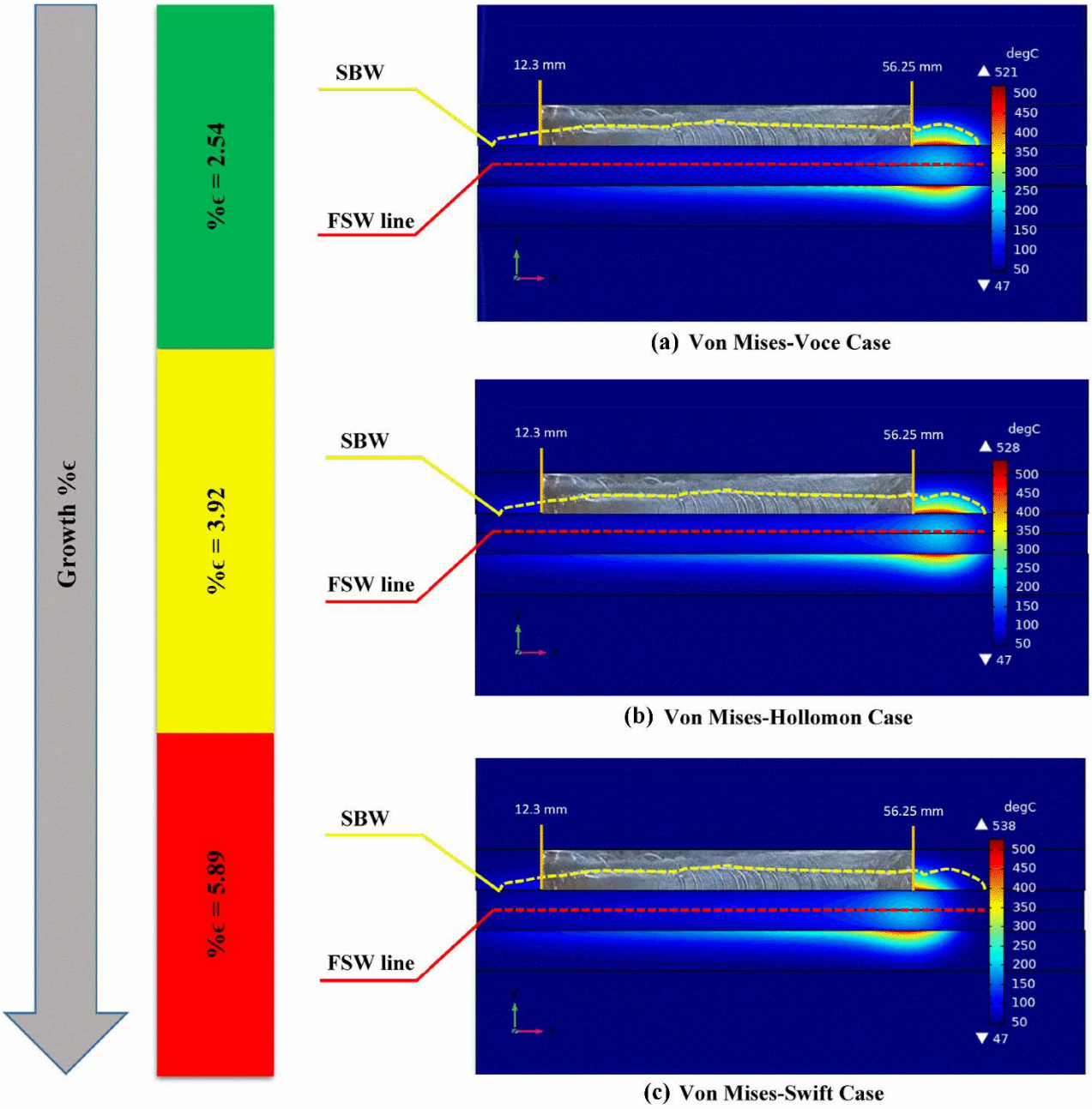


Fig. 10. Growth of error ratio resulting from peak temperature of FSW for Al 6061-T6 according to hybrid models of applied heat: (a) Von Mises-Voce, (b) Von Mises-Hollomon, and (c) Von Mises-Swift. Yellow color: Shoulder Boundary Waves (SBW) and red color: FSW line

Depending on these outcomes, the thermal history presented by TC1-TC6 and peak temperature according to Eq. (48) were firmly validated with the simulation results utilizing the hybrid model of thermal applied in Eq. (46) according to Von Mises-Voce compared to other hybrid models. Consequently, this hybrid model has achieved the best results with experimental data of FSW for Al 6061-T6. Whereby the Von Mises-Voce model presented a significant annealing behavior with slight strain-hardening. Besides, the previous Gaussian models for heat flux in FSW did not adopt the constitutive models of yield strength and avoided the confidence and standard deviation ratios for normal distribution. Hence, these observed implications have been avoided by the Von Mises-Voce model to develop a more stable model for moving the heat source of FSW operation while considering the strain-hardening behavior in the plastic deformation occurring as a result of plunging and driving the pin tool over the workpiece. Accordingly, the welded cross-section in Fig. 11 can reflect the sobriety of outcomes. This section represents the time and the peak temperature zone in the present work. Therefore, the specific part on the right side in Fig. 11 refers to the simulated section at 8.7 min based on the Von Mises-Voce model, while the left hand reflects the morphology section at scaled

3 mm. Hence, this comparison demonstrated in Fig. 11 is immensely efficacious and boosts the outputs of the current study.

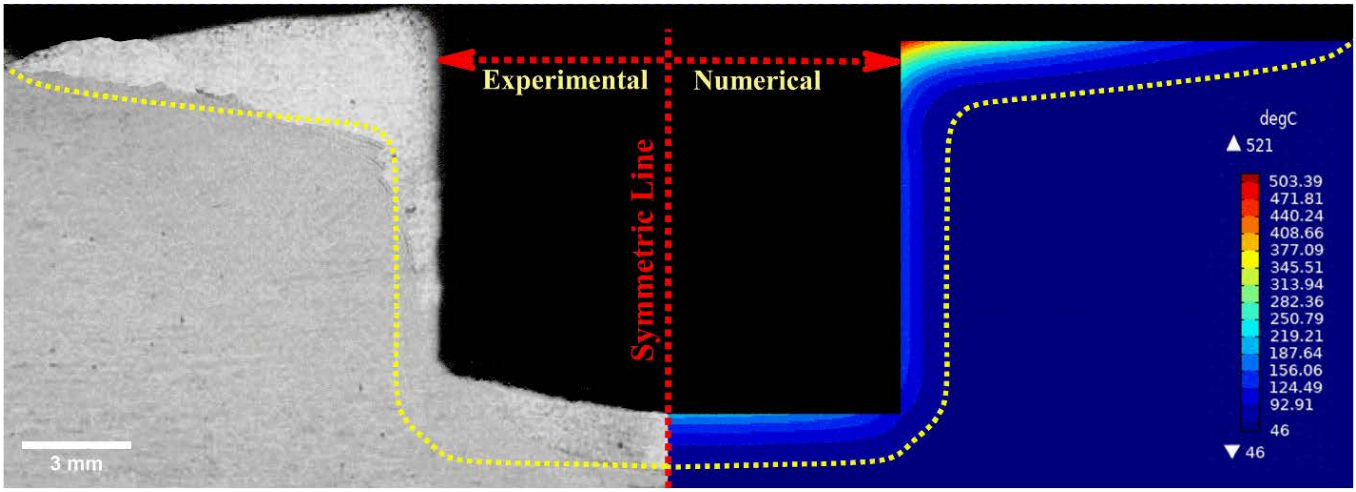


Fig. 11. Comparison of the plunged cross-sectional at 8.7 min for FSW of Al 6061-T6. Observed each half-section: The right section for the morphological structure of the welded part and the left hand for the simulation part of the welded section based on FEA

Based on these outputs, the role of the Von Mises-Voce model, as a significant hybrid model for frictional heat flow in FSW operation, can be observed by accurately predicting the thermal history depending on confidence and deviation ratios according to GD, besides Von Mises criterion, and constitutive models of yield strength. Nevertheless, both operational and geometrical indications influence the performance of this hybrid model as limitations to this hybrid model. Operationally, the radiuses of the pin and shoulder for the tool, besides the pin height, are essential parameters referring to the contacted surface area of the workpiece during plunging in the FSW process [33,77]. On the other hand, the rotational speed and normal force are dynamic variables related to plastic deformation for the Nugget zone [78]. Hence, these indications can be observed in Eq. (46) for the Von Mises-Voce model. Therefore, the positive control by these indications boosts the efficiency of this model. From here, this positive controlling of these indications for the Von Mises-Voce model can aid in the design study and optimization by application (Topology Optimization) as a significant tool in FSW [79]. Therefore, this tool in FSW can employ RAMP (Regularized Assumed Material Properties), SIMP (Solid Isotropic Material with Penalization), ESO (Evolutionary Structural Optimization), or TOSCA (Topology Optimization Software for Computer Aided Engineering) algorithm to enhance the material distribution topology according to the best scenario of the design study [80]. In addition, the principle of DFM (Design for Manufacturing) enhances the selection of suitable materials and operations in FSW [81]. In summary, topology optimization and DFM are valuable tools to develop this hybrid model in future work. Furthermore, the plunged depth as an equivalent parameter to pin depth in the friction stir spot welding (FSSW) operation is an active significant cartesian dimension in the heat flow simulation resulting from friction between the pin tool and workpiece [82,83]. Hence, it can propose the Von Mises-Voce model and neglect the other cartesian coordinates for the tool path in Eq. (47) as an essential limitation in this friction welding technology. Accordingly, it is significant to adapt the operational and geometrical parameters for Eq. (46) to be accepted with the other applications of FSW.

Observably, the employing confidence level and standard deviation in GD with the constitutive models for yield strength in the present work has contributed to earning a unique hybrid model of Von Mises-Voce since it dealt with the role of strain hardening behavior during FSW operation as compared to other researches, as demonstrated in Table 1. Therefore, the outcomes of the error ratio in the previous studies for the peak temperature were 5%-19%, where these studies adopted ALE (Arbitrary Lagrangian-Euleraian)-Explicit, SSHT, and Transient-DFLUX modes, as compared to the results of the current study [72,84-88]. Thus, this hybrid model has predictively proved to outperform the outcomes of these researches, where, as mentioned above, it produced 2.54% as an error ratio for peak temperature. Accordingly, the geometrical and operational indications for the Von Mises-Voce model are considered points of convergence with these studies. However, as aforementioned, the deviation and confidence ratios adopted besides the Voce model for yield strength with Von Mises led to boosting the current heat flux model based on the GD principle. As a result, these significant aspects improved the accuracy and realism of the predicted thermal history from the FSW path. Finally, the predictive and experimental outcomes of the current work have proved the feasibility of the Von Mises-Voce model as a hybrid heat flux in the FSW process. Hence, this model can be exploited to interpret the thermal history of the extruded aluminum utilized to produce the bulkheads and decks in the naval structures since this type of aluminum (6061-T6) possesses high strength, where it suffers from strain hardening obstacles during FSW operation [89-92].

## *5 CONCLUSIONS*

As a path of FSW operation for Al 6061-T6, the moving heat source is deemed an essential obstacle in the numerical model. Therefore, this study presented unified hybrid models for treating the friction and plastic deformation

generated during this operation to avoid this challenge. For the heat friction obstacle, these hybrid models employed 0.25% and 99.75% as deviation and confidence percentages in GD, respectively, for the moving heat source as a thermal applied load. Furthermore, the constitutive models were also utilized with GD function depending on Von Mises's criterion to overcome the plastic deformation issues. Hence, under the Von Mises-Voce, Von Mises-Hollomon, and Von Mises-Swift, as hybrid models, by utilizing 800 rpm, 10 mm/min, and 15 kN as experimental conditions, the thermal history concluded the following:

i. The thermal history measured by thermocouple sensors TC1 to TC6 was validated by the thermal predicted data achieved by FEA simulation utilizing Prob-Points P-1 to P-6 according to the hybrid models Von Mises-Voce, Von Mises-Swift, and Von Mises-Hollomon. Hence, the Von Mises-Voce model was dominant compared to other proposed hybrid models, where the error ratios of this model did not exceed 9.891% and 8.550% for the maximum and average temperatures consecutively.

ii. The peak temperature for FSW of Al 6061-T6 according to the Von Mises-Voce model has proved best to validate the Arbegast and Hartley model at ~ 2.54% error ratio than other hybrid models of heat applied in the present work that did not exceed 6%.

These concluded outputs indicate a pivotal contribution to stabilizing the welding process by adopting confidence and deviation ratios in GD, besides utilizing the constitutive models for yield strength. Hence, the findings from this study emphasize the significant dominance of the Von Mises-Voce model in the performance of thermal predictive in the FSW operation as compared to other hybrid models since the strain-hardening behavior is linear and homogeneous. Moreover, the implications of the outcomes of this study can be exploited in the structures of naval and airplanes, especially in bulkheads, decks, and fuselages, to predict thermal history for FSW by observing the suitable rotational and linear speed that is supplying the best annealing with reducing strain hardening behavior for Al 6061-T6.

In summary, this study offers the best hybrid employing GD principles with constitutive models for yield strength, specifically targeting FSW operation, where it has proven effective, opening new opportunities for their application in other fields of welding friction techniques.

## 6 ACKNOWLEDGEMENT

The authors would like to express their profound gratitude and deepest appreciation to the Ministry of Higher Education and Scientific Research, Iraq. Furthermore, the authors would like to express their special thanks to Sustainable Manufacturing and Recycling Technology-Advanced Manufacturing and Materials Centre (SMART-AMMC), University Tun Hussein Onn Malaysia (UTHM), Malaysia, besides Kut Technical Institute-Middle Technical University, and Engineering Technical College-Najaf/Al-Furat Al-Awsat Technical University (ATU).

## 7 AUTHOR CONTRIBUTION STATEMENT

Ghassan Shaker Abdul Ridha implemented the experimental performance. Mohammed Abdulridha Abbas is the corresponding author who implemented the experimental performance, wrote the manuscript, made grammatical corrections, collected data, performed simulations, and proposed the hybrid models. Ramin Hashemi, Mohd Amri Lajis, and Muhannad Ahmed revised the manuscript's content.

## 8 REFERECES

[1] Roberts, C. E., Bourell, D., Watt, T., Cohen, J., (2016). A novel processing approach for additive manufacturing of commercial aluminum alloys. Physics Procedia, 909-917.

[2] Walde, C., Cote, D., Champagne, V., Sisson, R. (2019). Characterizing the effect of thermal processing on feedstock Al alloy powder for additive manufacturing applications. *Journal of Materials Engineering and Performance*, vol. 28, no. 2, 601-610, DOI: 10.1007/s11665-018-3550-0

[3] Woo, W., Feng, Z., Wang, X.-L., Brown, D., Clausen, B., An, K., Choo, H., Hubbard, C. R., David, S. A. (2007). In situ neutron diffraction measurements of temperature and stresses during friction stir welding of 6061-T6 aluminium alloy. *Science and Technology of Welding and Joining*, vol. 12, no. 4, 298-303, DOI: 10.1179/174329307X197548

[4] Hwang, Y.-M., Kang, Z.-W., Chiou, Y.-C., Hsu, H.-H. (2008). Experimental study on temperature distributions within the workpiece during friction stir welding of aluminum alloys. *International Journal of Machine Tools and Manufacture*, vol. 48, no. 7-8, 778-787, DOI: 10.1016/j.ijmachtools.2007.12.003

[5] Ji, S., Meng, X., Ma, L., Gao, S. (2016). Effect of groove distribution in shoulder on formation, macrostructures, and mechanical properties of pinless friction stir welding of 6061-O aluminum alloy. *The International Journal of Advanced Manufacturing Technology*, vol. 87, no. 3051-3058, DOI: 10.1007/s00170-016-8734-x

[6] Liu, X., Sun, Y., Morisada, Y., Fujii, H. (2018). Dynamics of rotational flow in friction stir welding of aluminium alloys. *Journal of Materials Processing Technology*, vol. 252, no. 643-651, DOI: 10.1016/j.jmatprotec.2017.10.033

[7] Nourani, M., Milani, A., Yannacopoulos, S. (2015). On experimental optimization of friction stir welding of aluminum 6061: understanding processing-microstructure-property relations. *The International Journal of Advanced Manufacturing Technology*, vol. 79, no. 1425-1441, DOI: 10.1007/s00170-015-6932-6

[8] Trueba, L., Torres, M. A., Johannes, L. B., Rybicki, D. (2018). Process optimization in the self-reacting friction stir welding of aluminum 6061-T6. *International Journal of Material Forming*, vol. 11, no. 559-570, DOI: 10.1007/s12289-017-1365-4

[9] Fathi, J., Ebrahimzadeh, P., Farasati, R., Teimouri, R. (2019). Friction stir welding of aluminum 6061-T6 in presence of watercooling: Analyzing mechanical properties and residual stress distribution. *International Journal of Lightweight Materials and Manufacture*, vol. 2, no. 2, 107-115, DOI: 10.1016/j.ijlmm.2019.04.007

[10] Singh, A. K., Sahlot, P., Paliwal, M., Arora, A. (2019). Heat transfer modeling of dissimilar FSW of Al 6061/AZ31 using experimentally measured thermo-physical properties. *The International Journal of Advanced Manufacturing Technology*, vol. 105, no. 771-783, DOI: 10.1007/s00170-019-04276-y

[11] Hema, P. (2019). Experimental investigations on AA 6061 alloy welded joints by friction stir welding. Cooke, K. O. (Eds.), Aluminium Alloys and Composites. IntechOpen, Croatia, 133.

[12] Montes-González, F. A., Rodríguez-Rosales, N. A., Ortiz-Cuellar, J. C., Muñiz-Valdez, C. R., Gómez-Casas, J., Galindo-Valdés, J. S., Gómez-Casas, O. (2021). Experimental analysis and mathematical model of fsw parameter effects on the corrosion rate of Al 6061-T6-Cu c11000 joints. *Crystals*, vol. 11, no. 3, 294, DOI: 10.3390/cryst11030294

[13] Rajesh Jesudoss Hynes, N., Vivek Prabhu, M., Shenbaga Velu, P., Kumar, R., Tharmaraj, R., Farooq, M. U., Pruncu, C. I. (2022). An experimental insight of friction stir welding of dissimilar AA 6061/Mg AZ 31 B joints. *Proceedings of the Institution of Mechanical Engineers, Part B: Journal of Engineering Manufacture*, vol. 236, no. 6-7, 787-797, DOI: 10.1177/09544054211043474

[14] Abbasi, M., Bagheri, B., Keivani, R. (2015). Thermal analysis of friction stir welding process and investigation into affective parameters using simulation. *Journal of Mechanical Science and Technology*, vol. 29, no. 861-866, DOI: 10.1007/s12206-015-0149-3

[15] Ajri, A., Rohatgi, N., Shin, Y. C. (2020). Analysis of defect formation mechanisms and their effects on weld strength during friction stir welding of Al 6061-T6 via experiments and finite element modeling. *The International Journal of Advanced Manufacturing Technology*, vol. 107, no. 4621-4635, DOI: 10.1007/s00170-020-05353-3

[16] Assidi, M., Fourment, L., Guerdoux, S., Nelson, T. (2010). Friction model for friction stir welding process simulation: Calibrations from welding experiments. *International Journal of Machine Tools and Manufacture*, vol. 50, no. 2, 143-155, DOI: 10.1016/j.ijmachtools.2009.11.008

[17] Jabbari, M. (2013). Effect of the preheating temperature on process time in friction stir welding of Al 6061-T6. *Journal of Engineering*, vol. 2013, no. DOI: 10.1155/2013/580805

[18] Liu, X., Chen, G., Ni, J., Feng, Z. (2017). Computational fluid dynamics modeling on steady-state friction stir welding of aluminum alloy 6061 to TRIP steel. *Journal of Manufacturing Science and Engineering*, vol. 139, no. 5, 051004, DOI: 10.1115/1.4034895

[19] Vargas, J. A., Torres, J. E., Pacheco, J. A., Hernandez, R. J. (2013). Analysis of heat input effect on the mechanical properties of Al-6061-T6 alloy weld joints. *Materials & Design (1980-2015)*, vol. 52, no. 556-564, DOI: 10.1016/j.matdes.2013.05.081

[20] Pamuk, M. T., Savaş, A., Seçgin, Ö., Arda, E. (2018). Numerical simulation of transient heat transfer in friction-stir welding. *International Journal on Heat and Technology*, vol. no. DOI: 10.18280/ijht.360104

[21] Song, M. Kovacevic, R. (2003). Numerical and experimental study of the heat transfer process in friction stir welding. *Proceedings of the Institution of Mechanical Engineers, Part B: Journal of Engineering Manufacture*, vol. 217, no. 1, 73-85, DOI: 10.1243/095440503762502297

[22] Song, M. Kovacevic, R. (2003). Thermal modeling of friction stir welding in a moving coordinate system and its validation. *International Journal of machine tools and manufacture*, vol. 43, no. 6, 605-615, DOI: 10.1016/S0890-6955(03)00022-1

[23] Feng, Z., Wang, X.-L., David, S. A., Sklad, P. S. (2007). Modelling of residual stresses and property distributions in friction stir welds of aluminium alloy 6061-T6. *Science and Technology of Welding and Joining*, vol. 12, no. 4, 348-356, DOI: 10.1179/174329307X197610

[24] Chao, Y. J., Liu, S., Chien, C. H. (2008). Friction stir welding of al 6061-T6 thick plates: Part II-numerical modeling of the thermal and heat transfer phenomena. *Journal of the Chinese Institute of Engineers*, vol. 31, no. 5, 769-779, DOI: 10.1080/02533839.2008.9671431

[25] Atharifar, H., Lin, D., Kovacevic, R. (2009). Numerical and experimental investigations on the loads carried by the tool during friction stir welding. *Journal of Materials Engineering and Performance*, vol. 18, no. 339-350, DOI: 10.1007/s11665-008-9298-1

[26] Yang, C., Wu, C., Lv, X. (2018). Numerical analysis of mass transfer and material mixing in friction stir welding of aluminum/magnesium alloys. *Journal of Manufacturing Processes*, vol. 32, no. 380-394, DOI: 10.1016/j.jmapro.2018.03.009

[27] Zhang, J., Shen, Y., Li, B., Xu, H., Yao, X., Kuang, B., Gao, J. (2014). Numerical simulation and experimental investigation on friction stir welding of 6061-T6 aluminum alloy. *Materials & Design*, vol. 60, no. 94-101, DOI: 10.1016/j.matdes.2014.03.043

[28] Mohamadreza, N., Abbas S, M., Spiro, Y. (2011). Taguchi optimization of process parameters in friction stir welding of 6061 aluminum alloy: A review and case study. *Engineering*, vol. 2011, no. DOI: 10.4236/eng.2011.32017

[29] Raouache, E., Driss, Z., Guidara, M., Khalfallah, F. (2016). Effect of the tool geometries on thermal analysis of the friction stir welding. *International Journal of Mechanics and Applications*, vol. 6, no. 1, 1-7, DOI: 10.5923/j.mechanics.20160601.01

[30] Riahi, M. Nazari, H. (2011). Analysis of transient temperature and residual thermal stresses in friction stir welding of aluminum alloy 6061-T6 via numerical simulation. *The International Journal of Advanced Manufacturing Technology*, vol. 55, no. 143-152, DOI: 10.1007/s00170-010-3038-z

[31] Liu, X., Lan, S., Ni, J. (2015). Thermal mechanical modeling of the plunge stage during friction-stir welding of dissimilar Al 6061 to TRIP 780 steel. *Journal of manufacturing science and engineering*, vol. 137, no. 5, 051017, DOI: 10.1115/1.4031188

[32] Salloomi, K. N. (2019). Fully coupled thermomechanical simulation of friction stir welding of aluminum 6061-T6 alloy T-joint. *Journal of Manufacturing Processes*, vol. 45, no. 746-754, DOI: 10.1016/j.jmapro.2019.06.030

[33] Neto, D. M. Neto, P. (2013). Numerical modeling of friction stir welding process: a literature review. *The International Journal of Advanced Manufacturing Technology*, vol. 65, no. 115-126, DOI: 10.1007/s00170-012-4154-8

[34] Esmaeili, A., Besharati Givi, M., Zareie Rajani, H. (2012). Experimental investigation of material flow and welding defects in friction stir welding of aluminum to brass. *Materials and Manufacturing Processes*, vol. 27, no. 12, 1402-1408, DOI: 10.1080/10426914.2012.663239

[35] Sun, Y., Fujii, H., Takaki, N., Okitsu, Y. (2013). Microstructure and mechanical properties of dissimilar Al alloy/steel joints prepared by a flat spot friction stir welding technique. *Materials & design*, vol. 47, no. 350-357, DOI: 10.1016/j.matdes.2012.12.007

[36] Jun, C., Li, F.-g., SUN, Z.-k. (2017). Tensile stress–strain behavior of metallic alloys. *Transactions of Nonferrous Metals Society of China*, vol. 27, no. 11, 2443-2453, DOI: 10.1016/S1003-6326(17)60271-1

[37] Suryawanshi, J., Singh, G., Msolli, S., Jhon, M. H., Ramamurty, U. (2021). Tension-compression asymmetry and shear strength of titanium alloys. *Acta Materialia*, vol. 221, no. 117392, DOI: 10.1016/j.actamat.2021.117392

[38] Moore, J., Bibby, M., Goldak, J., Santyr, S., (1985). A comparison of the point source and finite element schemes for computing weld cooling. Joining division council university research symposium. 5. 1985 International welding congress, 1-9.

[39] Sabari, S. S., Malarvizhi, S., Balasubramanian, V., Reddy, G. M. (2016). Experimental and numerical investigation on under-water friction stir welding of armour grade AA2519-T87 aluminium alloy. *Defence Technology*, vol. 12, no. 4, 324-333, DOI: 10.1016/j.dt.2016.02.003

[40] Çengel, Y. A. (2009). *Introduction to Thermodynamics and Heat Transfer*. McGraw-Hill,

[41] Çengel, Y. A. Ghajar, A. J. (2019). *Heat and Mass Transfer: Fundamentals & Applications*. McGraw-Hill Education,

[42] Ozisik, M. N., McGraw-Hill Latinoamericana. Transferencia de calor, from *https://www.worldcat.org/title/transferencia-de-calor/oclc/730290212*, accessed on 5-9-2023.

[43] Engineers, A. I. o. C. (1990). *Properties and Selection: Nonferrous Alloys and Special-Purpose Materials*. American Institute of Chemical Engineers,

[44] Howard E. Boyer, T. L. G. (1985). *Handbook, ASM Metals*. American Society for Metals, Metals Park, Ohio,

[45] Totten, G. E. MacKenzie, D. S. (2003). *Handbook of Aluminum: Volume 2: Alloy production and materials manufacturing*. CRC press,

[46] Wong, J. C. (2008). *The correspondence between experimental data and computer simulation of friction stir welding (FSW)*. West Virginia University,

[47] Spencer, A. J. M. (2004). *Continuum mechanics*. Courier Corporation,

[48] Papoulis, A. (1991). *Random variables and stochastic processes*. McGraw Hill,

[49] Papoulis, A. Unnikrishna Pillai, S. (2002). *Probability, random variables and stochastic processes*.

[50] Cox, D. R. (2018). *Applied statistics-principles and examples*. Routledge,

[51] Lane, D. M., Scott, D., Hebl, M., Guerra, R., Osherson, D., Zimmer, H. (2017). Introduction to statistics, online edition. *Rice University, University of Houston Clear Lake, and Tufts University*, vol. no.

[52] Dorbane, A., Ayoub, G., Mansoor, B., Hamade, R., Imad, A. (2017). Effect of temperature on microstructure and fracture mechanisms in friction stir welded Al6061 joints. *Journal of Materials Engineering and Performance*, vol. 26, no. 2542-2554.

[53] Kaid, M., Zemri, M., Brahami, A., Zahaf, S. (2019). Effect of friction stir welding (FSW) parameters on the peak temperature and the residual stresses of aluminum alloy 6061-T6: Numerical modelisation. *International Journal on Interactive Design and Manufacturing (IJIDeM)*, vol. 13, no. 797-807.

[54] Zina, N., Zahaf, S., Bouaziz, S. A., Brahami, A., Kaid, M., Chetti, B., Najafi Vafa, Z. (2019). Numerical simulation on the effect of friction stir welding parameters on the peak temperature, von Mises stress, and residual stresses of 6061-T6 aluminum alloy. *Journal of Failure Analysis and Prevention*, vol. 19, no. 1698-1719.

[55] Heumann, C. Shalabh, M. S. (2016). *Introduction to statistics and data analysis*. Springer,

[56] Lee, B., Yoon, S., Lee, J. W., Kim, Y., Chang, J., Yun, J., Ro, J. C., Lee, J.-S., Lee, J. H. (2020). Statistical characterization of the morphologies of nanoparticles through machine learning based electron microscopy image analysis. *ACS nano*, vol. 14, no. 12, 17125-17133.

[57] Ott, R. Longnecker, M. (2010). *An introduction to statistical methods and data analysis*. Cengage Learning Inc.,

[58] Cheng, J., Ling, Y., De Waele, W. (2024). An ANN Hardness Prediction Tool Based on a Finite Element Implementation of a Thermal–Metallurgical Model for Mild Steel Produced by WAAM. *Metals*, vol. 14, no. 5, 556.

[59] Meng, Z., Cai, Z., Feng, J., Ma, H., Zhang, H., Li, S. (2024). Braille Character Segmentation Algorithm Based on Gaussian Diffusion. *Computers, Materials & Continua*, vol. 79, no. 1.

[60] Al-Roubaiy, A. O., Nabat, S. M., Batako, A. D. (2014). Experimental and theoretical analysis of friction stir welding of Al–Cu joints. *The International Journal of Advanced Manufacturing Technology*, vol. 71, no. 1631-1642, DOI: 10.1007/s00170-013-5563-z

[61] Guo, J., Chen, H., Sun, C., Bi, G., Sun, Z., Wei, J. (2014). Friction stir welding of dissimilar materials between AA6061 and AA7075 Al alloys effects of process parameters. *Materials & Design (1980-2015)*, vol. 56, no. 185-192, DOI: 10.1016/j.matdes.2013.10.082

[62] Jin, Z., Minerals, M., Meeting, M. S., Minerals, M., Shaping, M. S., Committee, F. (2003). *Hot Deformation of Aluminum Alloys III: 2003 TMS Annual Meeting, San Diego, California, March 2-6, 2003*. TMS, University of Michigan.

[63] Las-Casas, M. S., de Ávila, T. L. D., Bracarense, A. Q., Lima, E. J. (2018). Weld parameter prediction using artificial neural network: FN and geometric parameter prediction of austenitic stainless steel welds. *Journal of the Brazilian Society of Mechanical Sciences and Engineering*, vol. 40, no. 1-9.

[64] Panda, B. N., Babhubalendruni, M. R., Biswal, B. B., Rajput, D. S., (2015). Application of artificial intelligence methods to spot welding of commercial aluminum sheets (BS 1050). Proceedings of Fourth International Conference on Soft Computing for Problem Solving: SocProS 2014, Volume 1, 21-32.

[65] Cabibbo, M., Paoletti, C., Ghat, M., Forcellese, A., Simoncini, M. (2019). Post-FSW cold-rolling simulation of ECAP shear deformation and its microstructure role combined to annealing in a FSWed AA5754 plate joint. *Materials*, vol. 12, no. 9, 1526.

[66] Jia, C., Wu, L., Xue, P., Ni, D., Xiao, B., Ma, Z. (2022). Effect of static annealing on superplastic behavior of a friction stir welded Ti-6Al-4V alloy joint and microstructural evolution during deformation. *Journal of Materials Science & Technology*, vol. 130, no. 112-123.

[67] Xia, Y., Yang, W., Yu, Y., Teng, H., Cheng, Q. (2023). Study of Flow Stress Models and Ductile Fracture Criteria for CHN327 Nickel-Based Superalloy. *Materials*, vol. 16, no. 6, 2232, DOI: 10.3390/ma16062232

[68] Fahimpour, V., Sadrnezhaad, S., Karimzadeh, F. (2012). Corrosion behavior of aluminum 6061 alloy joined by friction stir welding and gas tungsten arc welding methods. *Materials & Design*, vol. 39, no. 329-333, DOI: 10.1016/j.matdes.2012.02.043

[69] Liu, T.-S., Qiu, F., Yang, H.-Y., Shu, S.-L., Xie, J.-F., Jiang, Q.-C., Zhang, L.-C. (2023). Insights into the influences of nanoparticles on microstructure evolution mechanism and mechanical properties of friction-stir-welded Al 6061 alloys. *Materials Science and Engineering: A*, vol. 871, no. 144929, DOI: 10.1016/j.msea.2023.144929

[70] Rathinasuriyan, C. Kumar, V. S. (2017). Experimental investigation of weld characteristics on submerged friction stir welded 6061-T6 aluminum alloy. *Journal of Mechanical Science and Technology*, vol. 31, no. 3925-3933, DOI: 10.1007/s12206-017-0738-4

[71] Hamilton, C., Sommers, A., Dymek, S. (2009). A thermal model of friction stir welding applied to Sc-modified Al–Zn–Mg–Cu alloy extrusions. *International Journal of Machine Tools and Manufacture*, vol. 49, no. 3-4, 230-238, DOI: 10.1016/j.ijmachtools.2008.11.004

[72] Jamshidi Aval, H., Serajzadeh, S., Kokabi, A. (2012). Experimental and theoretical evaluations of thermal histories and residual stresses in dissimilar friction stir welding of AA5086-AA6061. *The International Journal of Advanced Manufacturing Technology*, vol. 61, no. 149-160, DOI: 10.1007/s00170-011-3713-8

[73] Mishra, R. S. Ma, Z. (2005). Friction stir welding and processing. *Materials science and engineering: R: reports*, vol. 50, no. 1-2, 1-78.

[74] Arbegast, W. Hartley, P. (1999). Friction stir weld technology development at Lockheed Martin Michoud Space System--an overview. *ASM International, Trends in Welding Research(USA)*, vol. no. 541-546.

[75] Bisadi, H., Rasaee, S., Farahmand, M. (2014). Effects of pin shape on the tool plunge stage in friction stir welding. *Transactions of the Indian Institute of Metals*, vol. 67, no. 989-995, DOI: 10.1007/s12666-014-0421-8

[76] Fehrenbacher, A., Duffie, N. A., Ferrier, N. J., Pfefferkorn, F. E., Zinn, M. R. (2014). Effects of tool–workpiece interface temperature on weld quality and quality improvements through temperature control in friction stir welding. *The International Journal of Advanced Manufacturing Technology*, vol. 71, no. 165-179, DOI: 10.1007/s00170-013-5364-4

[77] Padhy, G., Wu, C., Gao, S. (2018). Friction stir based welding and processing technologies-processes, parameters, microstructures and applications: A review. *Journal of Materials Science & Technology*, vol. 34, no. 1, 1-38.

[78] Anand, R. Sridhar, V. (2020). Studies on process parameters and tool geometry selecting aspects of friction stir welding–A review. *Materials Today: Proceedings*, vol. 27, no. 576-583.

[79] Harston, S., Mattson, C., Koecher, M., (2010). A topology optimization method with anisotropic materials. 13th AIAA/ISSMO Multidisciplinary Analysis Optimization Conference, 9176.

[80] Luo, H., Fu, J., Wang, P., Liu, J., Zhou, W. (2020). Design optimization of the ram structure of friction stir welding robot. *Mechanics of Advanced Materials and Structures*, vol. 27, no. 2, 108-118.

[81] Bagaitkar, H. Allada, V., (2008). Design for Manufacturing (DFM) Methodology to Implement Friction Stir Welding (FSW) for Automobile Chassis Fabrication. International Design Engineering Technical Conferences and Computers and Information in Engineering Conference, 219-226.

[82] Hannachi, N., Khalfallah, A., Leitão, C., Rodrigues, D. (2022). Thermo-mechanical modelling of the Friction Stir Spot Welding process: Effect of the friction models on the heat generation mechanisms. *Proceedings of the Institution of Mechanical Engineers, Part L: Journal of Materials: Design and Applications*, vol. 236, no. 8, 1464-1475.

[83] Kim, D., Badarinarayan, H., Ryu, I., Kim, J. H., Kim, C., Okamoto, K., Wagoner, R., Chung, K. (2010). Numerical simulation of friction stir spot welding process for aluminum alloys. *Metals and Materials International*, vol. 16, no. 323-332.

[84] Casavola, C., Cazzato, A., Moramarco, V., Pappalettere, C., (2015). Temperature field in FSW process: experimental measurement and numerical simulation. Experimental and Applied Mechanics, Volume 6: Proceedings of the 2014 Annual Conference on Experimental and Applied Mechanics, 177-186.

[85] Meyghani, B., Awang, M. B., Poshteh, R. G. M., Momeni, M., Kakooei, S., Hamdi, Z., (2019). The effect of friction coefficient in thermal analysis of friction stir welding (FSW). IOP Conference series: materials science and engineering, 012102.

[86] Pankaj, P., Tiwari, A., Biswas, P., Rao, A. G. (2021). Plasma-assisted hybrid dissimilar friction stir welding for joining of DH36 steel and AISI 1008 steel: thermal modelling and experimental analysis. *Arabian Journal for Science and Engineering*, vol. 46, no. 7929-7952.

[87] Vasanthakumar, P., Sekar, K., Jayantherababu, J., (2019). Thermal prediction and experimental validation of Friction Stir Welded Aerospace Grade Aluminium Alloy. Journal of Physics: Conference Series, 012150.

[88] Yaduwanshi, D., Bag, S., Pal, S. (2016). Numerical modeling and experimental investigation on plasma-assisted hybrid friction stir welding of dissimilar materials. *Materials & Design*, vol. 92, no. 166-183.

[89] Kesharwani, R., Jha, K. K., Imam, M., Sarkar, C., Barsoum, I. (2023). Comparison of microstructural, texture and mechanical properties of SiC and Zn particle reinforced FSW 6061-T6 aluminium alloy. *Journal of Materials Research and Technology*, vol. 26, no. 3301-3321.

[90] Luo, D., Li, F., Xing, G. (2022). Corrosion resistance of 6061-T6 aluminium alloy and its feasibility of near-surface reinforcements in concrete structure. *Reviews on Advanced Materials Science*, vol. 61, no. 1, 638-653.

[91] Wahid, M. A., Siddiquee, A. N., Khan, Z. A. (2020). Aluminum alloys in marine construction: characteristics, application, and problems from a fabrication viewpoint. *Marine Systems & Ocean Technology*, vol. 15, no. 1, 70-80.

[92] Wilhelm, C., LaCaille, G., Wright, N., Ward, N., Shu, C., Painter, R., Vinquist, C., Stoyanov, P., Lee, E., Piatkowski, D. (2009). Mechanical properties and microstructure characterization of coated AM2 Al 6061-T6 mats exposed to simulated thermal blast. *Engineering Failure Analysis*, vol. 16, no. 1, 1-10.

## 9 LIST OF ABBREVIATIONS AND NOMENCLATURE

| | | | |
|---|---|---|---|
| *FEA* | Finite Element Analysis. | $v_l$ | Linear velocity of pin tool during FSW. |
| *FSW* | Friction Stir Welding. | $\varepsilon_o$ | Saturation of the strain according to Swift's model |
| *GD* | Gaussian Distribution. | $h_p$ | Pin height. |
| *TC* | Thermocouple sensor. | $k$ | Thermal conductivity of workpiece. |
| $h_l$ | Convection heat transfer coefficient for the lower surface of workpiece. | $Pr$ | Prandtl number. |
| $h_u$ | Convection heat transfer coefficient for the upper surface of workpiece. | $v_k$ | Kinematic viscosity. |
| $A_S$ | Cross-Sectional area of shoulder face. | $\rho$ | Density of workpiece. |
| $F_P$ | Force translated during FSW operation. | $C$ | Material coefficient according to Voce's model. |
| $F_n$ | Normal force applied on workpiece. | $Gr$ | Grashof number. |
| $K_h$ | Strength coefficient according Hollomon's model. | $P$ | Plunge pressure applied on pin tool. |
| $K_s$ | Strength coefficient according Swift's model. | $R$ | Distribution of heat friction for the curve's shoulder according to GD. |
| $Nu_l$ | Nusselt number for the upper surface of workpiece. | $Ra$ | Rayleigh number. |
| $Nu_u$ | Nusselt number for the lower surface of workpiece. | $T$ | Absorbed temperature produced from upper and lower surfaces of workpiece. |
| $Q_S$ | Heat source generated by shoulder surface. | $g$ | Constant of gravitational acceleration. |
| $Q_p$ | Heat source generated by pin surface. | $r$ | Random variable. |
| $Q_{in}$ | Total input energy flow generated from welding by stir friction mechanism. | $t$ | FSW duration. |
| $\delta_h$ | Contact variable state for the tool surface plunged. | $\delta$ | Characteristic length of the horizontal plate. |
| $\delta_C$ | Contact variable state for the bottom surface of pin tool. | $\eta$ | FSW efficiency. |
| $T_P$ | Peak temperature in the welding zone. | $\theta$ | Volume expansion coefficient. |
| $T_a$ | Ambient temperature. | $\lambda$ | Pin tool angle. |
| $T_m$ | Melting temperature of workpiece. | $\mu$ | Friction coefficient. |
| $T_o$ | Reference temperature. | $\sigma$ | Standard deviation according to GD. |
| $n_h$ | Strain-Hardening exponent according to Hollomon's model. | $\tau$ | Average shear stress. |
| $n_s$ | Strain-Hardening exponent according to Swift's model. | $\psi$ | Partition coefficient of heat friction. |
| $q_f$ | Heat flux generated by friction between workpiece and pin tool. | $\omega$ | Rotational velocity. |
| $q_{in}$ | Total heat flux input to the welding zone. | $\varepsilon_r$ | Emissivity factor for workpiece surface. |
| $q_p$ | Heat flux input to the welding zone by pin tool. | $\sigma_o$ | Saturation of stress according to Voce's model. |
| $q_{pd}$ | Heat flux generated from plastic deformation in the welding zone. | $\sigma_y$ | Yield strength for the workpiece. |
| $q_s$ | Heat flux input to the welding zone by shoulder. | $C_p$ | Specific heat of workpiece. |
| $r_S$ | Shoulder radius. | $h_d$ | Welding depth. |
| $r_p$ | Pin radius. | $t_w$ | Workpiece thickness. |

*Paper submitted: 13.09.2023.*
*Paper accepted: 21.02.2025.*